

# $\bar{K} + N \rightarrow K + \Xi$ reaction and $S = -1$ hyperon resonances

Benjamin C. Jackson,<sup>1</sup> Yongseok Oh,<sup>2,3,\*</sup> H. Haberzettl,<sup>4,†</sup> and K. Nakayama<sup>1,5,‡</sup>

<sup>1</sup>*Department of Physics and Astronomy, The University of Georgia, Athens, GA 30602, USA*

<sup>2</sup>*Department of Physics, Kyungpook National University, Daegu 702-701, Korea*

<sup>3</sup>*Asia Pacific Center for Theoretical Physics, Pohang, Gyeongbuk 790-784, Korea*

<sup>4</sup>*Institute for Nuclear Studies and Department of Physics,  
The George Washington University, Washington, DC 20052, USA*

<sup>5</sup>*Institut für Kernphysik and Center for Hadron Physics,  
Forschungszentrum Jülich, 52425 Jülich, Germany*

(Dated: October 31, 2018)

The  $\bar{K} + N \rightarrow K + \Xi$  reaction is studied for center-of-momentum energies ranging from threshold to 3 GeV in an effective Lagrangian approach that includes the hyperon  $s$ - and  $u$ -channel contributions as well as a phenomenological contact amplitude. The latter accounts for the rescattering term in the scattering equation and possible short-range dynamics not included explicitly in the model. Existing data are well reproduced and three above-the-threshold resonances were found to be required to describe the data, namely, the  $\Lambda(1890)$ ,  $\Sigma(2030)$ , and  $\Sigma(2250)$ . For the latter resonance we have assumed the spin-parity of  $J^P = 5/2^-$  and a mass of 2265 MeV. The  $\Sigma(2030)$  resonance is crucial in achieving a good reproduction of not only the measured total and differential cross sections, but also the recoil polarization asymmetry. More precise data are required before a more definitive statement can be made about the other two resonances, in particular, about the  $\Sigma(2250)$  resonance that is introduced to describe a small bump structure observed in the total cross section of  $K^- + p \rightarrow K^+ + \Xi^-$ . The present analysis also reveals a peculiar behavior of the total cross section data in the threshold energy region in  $K^- + p \rightarrow K^+ + \Xi^-$ , where the  $P$ - and  $D$ -waves dominate instead of the usual  $S$ -wave. Predictions for the target-recoil asymmetries of the  $\bar{K} + N \rightarrow K + \Xi$  reaction are also presented.

PACS numbers: 13.75.Jz, 13.60.Rj, 13.88.+e, 14.20.Jn

## I. INTRODUCTION

Hadron spectroscopy is an essential part of the investigation to understand the non-perturbative regime of Quantum Chromodynamics (QCD). In principle, an ab-initio approach to hadron resonance physics can be provided by lattice QCD simulations. In particular, the spectra of excited baryons observed in the recent lattice simulations [1, 2] hold the promise of explaining the rich dynamics in the resonance energy region in the near future. Once quark masses drop towards more reasonable values and finite volume effects are fully under control, a close comparison to experimental data will be possible. Other approaches such as the dynamical Dyson-Schwinger [3], constituent quark models [4, 5], and the Skyrme model [6] also generate resonance spectra. Unitarized Chiral Perturbation Theory also provides a complementary picture of some of the low-lying resonances [7, 8]. To compare these theoretical results with the experimental data, a reliable reaction theory capable of identifying resonances and extracting the corresponding resonance parameters is required. Such reaction theories, based on a coupled-channel approach, have been developed at various degrees of sophistication and are being

improved [9–16]. So far, most of the experimentally extracted baryon resonances come from the pion-induced reaction experiments, especially the  $\pi N$  scattering, and about 16 nucleon resonances and 11  $\Delta$  resonances have been identified [17]. A number of  $\Lambda$  and  $\Sigma$  baryons, which are particles with strangeness quantum number  $S = -1$ , have been also discovered [17]. A review on the status of baryon spectroscopy is given, e.g., in Ref. [18].

Although the multi-strangeness baryons ( $S < -1$ ) have played an important role in the development of our understanding of strong interactions, and thus, should be an integral part of any baryon spectroscopy program, the current knowledge of these baryons is still extremely limited. In fact, the SU(3) flavor symmetry allows as many  $S = -2$  baryon resonances, called  $\Xi$ , as there are  $N$  and  $\Delta$  resonances combined ( $\sim 27$ ); however, until now, only eleven  $\Xi$  baryons have been discovered [17]. Among them, only three [ground state  $\Xi(1318)1/2^+$ ,  $\Xi(1538)3/2^+$ , and  $\Xi(1820)3/2^-$ ] have their quantum numbers assigned.<sup>1</sup> This situation is mainly due to the fact that multi-strangeness particle productions have relatively low yields. For example, if there are no strange particles in the initial state,  $\Xi$  is produced only indirectly and the yield is only of the order of nb in the photoproduction reaction [19], whereas the yield

\* yohphy@knu.ac.kr

† helmut@gwu.edu

‡ nakayama@uga.edu

<sup>1</sup> The parity of the ground state  $\Xi$  has not been measured explicitly yet, but its assignment is based on quark models and SU(3) flavor symmetry.

is of the order of  $\mu\text{b}$  [20] in the hadronic  $\bar{K}$ -induced reaction, where the  $\Xi$  is produced directly because of the presence of an  $S = -1$   $\bar{K}$  meson in the initial state. The production rates for  $\Omega$  baryons with  $S = -3$  are much lower [21].

The study of multi-strangeness baryons has started to attract a renewed interest recently. Indeed, the CLAS Collaboration at Thomas Jefferson National Accelerator Facility (JLab) plans to initiate a  $\Xi$  spectroscopy program using the upgraded 12-GeV machine, and measure exclusive  $\Omega$  photoproduction for the first time [22]. Some data for the production of the  $\Xi$  ground state, obtained from the 6-GeV machine, are already available [19]. They were analyzed by some of the present authors [23, 24] within an effective Lagrangian approach. J-PARC is going to study the  $\Xi$  baryons via the  $\bar{K} + N \rightarrow K + \Xi$  process (which is the reaction of choice for producing  $\Xi$ ) in connection to its program proposal for obtaining information on  $\Xi$  hypernuclei spectroscopy. It also plans to study the  $\pi + N \rightarrow K + K + \Xi$  reaction as well as  $\Omega$  production [25, 26]. At the FAIR facility of GSI, the reaction  $\bar{p} + p \rightarrow \bar{\Xi} + \Xi$  will be studied by the PANDA Collaboration [27]. Quite recently, lattice QCD calculations of the baryon spectra, including those of  $\Xi$  and  $\Omega$  baryons, have also been reported, for example, in Refs. [1, 2].

In the present work, we concentrate on the production of  $S = -2$   $\Xi$  and, in particular, on the production reaction process of the ground state  $\Xi$ ,

$$\bar{K}(q) + N(p) \rightarrow K(q') + \Xi(p'), \quad (1)$$

where the arguments indicate the corresponding particle's on-shell four-momentum. This reaction has been studied experimentally mainly throughout the 60's [28–37], which was followed by several measurements made in the 70's and 80's [38–44]. The existing data are rather limited and suffer from large uncertainties. The total cross section and some of the differential cross section data are tabulated in Ref. [20]. We shall return to the discussion of these experimental data later on. Early theoretical attempts to understand the above reaction are very few and can be found in Refs. [45–49]. Recent calculations are reported by Sharov *et al.* [50] and by Shyam *et al.* [51]. The former authors have considered both the total and differential cross sections as well as the recoil polarization data in their analysis, while the latter authors have considered only the total cross section data, although they too have predicted the differential cross sections, mentioning that they found it difficult to use the differential cross section data [37] for several reasons. Although the analyses of Refs. [50, 51] are both based on very similar effective Lagrangian approaches, the number of  $S = -1$  hyperon resonances included in the intermediate state are different. While in Ref. [50] only the  $\Sigma(1385)$  and  $\Lambda(1520)$  are considered in addition to the above-threshold  $\Sigma(2030)$  and  $\Sigma(2250)$  resonances,<sup>2</sup>

in Ref. [51] eight of the 3- and 4-star  $\Lambda$  and  $\Sigma$  resonances with masses up to 2.0 GeV have been considered. While the authors of Ref. [50] pointed out the significance of the above-threshold resonances, the authors of Ref. [51] have found the dominance of the sub-threshold  $\Lambda(1520)$  resonance. Reaction (1) has been also considered quite recently by Magas *et al.* [52] within the coupled channels Unitarized Chiral Perturbation approach in connection to the issue of determining the parameters of the next-to-leading-order interactions. The authors of Ref. [52] have added the  $\Sigma(2030)$  and  $\Sigma(2250)$  resonances into their calculation to improve the fit quality to the total cross section data. Just recently, the Argonne-Osaka group [53] reported applying their Dynamical Coupled Channels approach to  $\bar{K}$ -induced two-body reactions for center-of-momentum (c.m.) energies up to  $W = 2.1$  GeV. In the reported work, both the total and differential cross sections were calculated, but the extracted resonance parameter values are not yet available.

We note here that the proper identification of resonances and the reliable extraction of their parameters requires detailed knowledge of the analytic structures of the scattering amplitude that, to date, can only be obtained through a full coupled-channel treatment, such as that of Ref. [53]. However, because the currently available data in the  $K\Xi$  channel are scarce and of low quality, they do not provide sufficient constraints for the model parameters to permit an in-depth analysis of that channel [53]. In this context, we mention that a coupled-channel partial-wave analysis of  $\bar{K}$ -induced reactions up to  $W = 2.1$  GeV has also been performed recently by the Kent State University group [56, 57] which includes the  $\bar{K}N$ ,  $\pi\Lambda$ ,  $\pi\Sigma$ ,  $\pi\Lambda(1520)$ ,  $\pi\Sigma(1385)$ ,  $\bar{K}^*N$ , and  $\bar{K}\Delta$  channels, but not the  $K\Xi$  channel.

Some of the model-independent aspects of the reaction (1) have been studied recently by the present authors [54, 55]. In the present work, we perform a model-dependent analysis of the existing data between threshold and a c.m. energy of 3 GeV based on an effective Lagrangian approach that includes a phenomenological contact amplitude which accounts for the rescattering contributions and/or unknown (short-range) dynamics that have not been included explicitly into the model. While the tree-level model presented here is not very sophisticated, it captures the essential aspects of the process in question. As such, the use of a simplified, yet efficient model is particularly well suited for a situation, such as for the reaction (1), where scarce and poor data prevent a more detailed and complete treatment. The present study is our first step toward building a more complete reaction model capable of reliably extracting the properties of hyperons from the forthcoming experimental data, in addition to providing some guidance for planning future experiments. One of the purposes of the present work is to search for a clearer evidence of the

<sup>2</sup> The production threshold energy for the reaction of Eq. (1) is

about 1813 MeV.

$S = -1$  hyperon resonances in reaction (1). However, we emphasize that our main interest here lies not so much in the accurate extraction of  $S = -1$  hyperon resonance parameters, but in an exploratory study to learn about the pertinent reaction mechanisms and, in particular, to identify the resonances that come out to be most relevant for the description of the existing  $\Xi$  production data. In fact, with the exception of the  $\Sigma(2250)$  resonance, whose mass was adjusted slightly to better reproduce the observed bump structure in the total cross section in the charged  $\Xi$  production, the masses and widths of the resonances incorporated here are taken from other sources, as explained in Sec. III below. Only the product of the coupling constants and the cutoff parameters in the corresponding form factors are adjusted in the present work.

The investigation of reaction (1) also impacts the study of  $\Xi$  hypernuclei, where the elementary process of Eq. (1) is an input for the models of hypernuclei productions [49, 58–60]. As mentioned before, there is a proposed program at J-PARC and eventually at GSI-FAIR to obtain information about the spectroscopy of  $\Xi$  hypernuclei through the antikaon-induced reactions on nuclear targets. Establishing the existence and properties of  $\Xi$  hypernuclei is of considerable importance for a number of reasons and the study of reaction (1) is an essential step to this end.

The present paper is organized as follows. In Sec. II, our model for describing reaction (1) is presented, with some technical details supplied in the Appendix. In Sec. III, the results of our model calculations are presented and discussed. Section IV contains our summary and conclusions.

## II. MODEL DESCRIPTION

The reaction amplitude,  $T$ , describing a two-body process like the reaction (1) is, in general, given by the Bethe-Salpeter equation,

$$T = V + VG_0T, \quad (2)$$

where  $V$  stands for the (two-body) meson-baryon irreducible (Hermitian) driving amplitude and  $G_0$  describes free relative meson-baryon motion. Note that the above equation represents, in principle, a coupled-channels equation in meson-baryon channel space. It can be recast into the pole and the non-pole parts as

$$T = T^{\text{P}} + T^{\text{NP}}, \quad (3)$$

where the non-pole part  $T^{\text{NP}}$  obeys

$$T^{\text{NP}} = V^{\text{NP}} + V^{\text{NP}}G_0T^{\text{NP}} \quad (4)$$

with

$$V^{\text{NP}} \equiv V - V^{\text{P}} \quad (5)$$

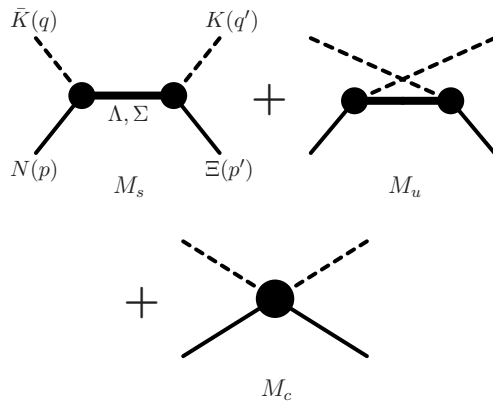


FIG. 1. Diagrams describing the amplitude (11) in the present calculation. The labeling of the external legs of the  $s$ -channel diagram,  $M_s$ , follows the reaction equation (1); the labels apply correspondingly also to the external legs of the  $u$ -channel diagram,  $M_u$ , and the contact term  $M_c$ . The intermediate hyperon exchanges,  $\Lambda$  and  $\Sigma$ , indicated for  $M_s$  also appear in  $M_u$ . The details of the contact amplitude,  $M_c$ , are discussed in Sec. II.

denoting the one-baryon irreducible (non-pole) part of the driving amplitude,  $V$ . Here,  $V^{\text{P}}$  stands for the one-baryon reducible (pole) part of  $V$  in the form of <sup>3</sup>

$$V^{\text{P}} = \sum_r |F_{0r}\rangle S_{0r} \langle F_{0r}|, \quad (6)$$

where  $|F_{0r}\rangle$  and  $S_{0r} = (p_r^2 - m_{0r}^2 + i0)^{-1}$  stand for the so-called bare vertex and bare baryon propagator, respectively. The summation runs over the baryons in the intermediate state, each specified by the index  $r$ . The four-momentum and the bare mass of the propagating baryon are denoted by  $p_r$  and  $m_{0r}$ , respectively. As can be seen in Fig. 1,  $V^{\text{P}}$  is the sum of the  $s$ -channel Feynman diagrams corresponding to bare baryon propagations in the intermediate state. The pole part of the reaction amplitude  $T^{\text{P}}$  in Eq. (3) is given by

$$T^{\text{P}} = \sum_{r'r} |F_{r'}\rangle S_{r'r} \langle F_r|, \quad (7)$$

where the so-called dressed vertex reads

$$\begin{aligned} |F_{r'}\rangle &= (1 + T^{\text{NP}}G_0) |F_{0r'}\rangle, \\ \langle F_r| &= \langle F_{0r}| (1 + G_0T^{\text{NP}}), \end{aligned} \quad (8)$$

and the dressed propagator  $S_{r'r}$  is written as

$$S_{r'r}^{-1} = S_{0r}^{-1} \delta_{r'r} - \Sigma_{r'r}, \quad (9)$$

with

$$\Sigma_{r'r} = \langle F_{0r'}| G_0 |F_r\rangle \quad (10)$$

\_\_\_\_\_

<sup>3</sup> The bra and ket notation here is used only as a quick visual cue to identify incoming and outgoing vertices, respectively. They are not to be taken as Hilbert space states in the usual sense.

denoting the self-energy.

In the present work we shall make the following approximations to the reaction amplitude in Eq. (3). First, we approximate the pole part of the reaction amplitude  $T^P$  by the  $s$ -channel Feynman amplitude,  $M_s$ , specified by effective Lagrangians and phenomenological Feynman propagators. Here, the dressed resonance coupling constants, dressed masses as well as the corresponding widths are parameters either fixed from independent sources or adjusted to reproduce the experimental data. The meson-baryon-baryon vertices are obtained from the effective Lagrangians given in the Appendix; the phenomenological Feynman propagators for dressed baryons are also found there. Note that, here, the resonance couplings in the dressed propagators are ignored.

Second, the non-pole part of the reaction amplitude  $T^{\text{NP}}$  is approximated as follows.

- (i) Since there is no meson-exchange  $t$ -channel process in the present reaction, unless the exchanged meson is an exotic one with strangeness quantum number  $S = 2$ ,  $V^{\text{NP}}$  of the reaction is approximated by the  $u$ -channel Feynman amplitude,  $M_u$ , constructed from the same effective Lagrangians and Feynman propagators used to construct the  $s$ -channel Feynman amplitudes.
- (ii) The rescattering term  $V^{\text{NP}}G_0T^{\text{NP}}$  in  $T^{\text{NP}}$  of Eq. (4) and other effects not explicitly included in the present approach are accounted for by a phenomenological contact term,  $M_c$ , which is specified below. This contact term will be discussed in more detail later.

With the approximations described above, the reaction amplitude in the present work is given by

$$T = M_s + M_u + M_c, \quad (11)$$

where  $M_s$  and  $M_u$  are the amplitudes from the  $s$ - and  $u$ -channel Feynman diagrams, respectively; both amplitudes include the ground-state hyperons as well as some of the  $S = -1$  hyperon resonances in the intermediate state. Figure 1 shows a diagrammatic representation of  $M_s$ ,  $M_u$ , and  $M_c$ .

The amplitude for the reaction of Eq. (1) can be decomposed into spin-non-flip and spin-flip contributions. Their respective partial-wave decomposed forms read<sup>4</sup>

$$\begin{aligned} M_{++} &= M_{--} \\ &= \frac{1}{4\pi} \sum_{L,T} \left[ (L+1) M_L^{TJ+}(p', p) + L M_L^{TJ-}(p', p) \right] \end{aligned}$$

$$\times P_L(\hat{\mathbf{p}} \cdot \hat{\mathbf{p}}') \hat{P}_T, \quad (12a)$$

$$\begin{aligned} M_{+-} &= -M_{-+} \\ &= \frac{1}{4\pi} \sum_{L,T} \left[ M_L^{TJ+}(p', p) - M_L^{TJ-}(p', p) \right] \\ &\quad \times P_L^1(\hat{\mathbf{p}} \cdot \hat{\mathbf{p}}') \hat{P}_T, \end{aligned} \quad (12b)$$

where initial and final momenta are as in Fig. 1. The indices  $s'$ ,  $s = \pm$  in  $M_{s's}$  stand for spin-up (+) and spin-down (-) of the final ( $s'$ ) and initial ( $s$ ) states quantized along the incoming momentum direction  $\hat{\mathbf{p}}$ , and  $J_{\pm} \equiv L \pm \frac{1}{2}$  (for  $L = 0$ , the corresponding  $J_{-}$  terms are zero).  $M_L^{TJ\pm}$  are diagonal elements of the more general partial-wave amplitudes introduced in Ref. [55] (where full technical details can be found). The Legendre and associated Legendre functions are denoted by  $P_L(x)$  and  $P_L^1(x)$ , respectively,<sup>5</sup> with argument  $\hat{\mathbf{p}} \cdot \hat{\mathbf{p}}' = \cos \theta$ , where  $\theta$  is the scattering angle. The total angular momentum, orbital angular momentum, and total isospin of the meson-baryon state are represented by  $J, L$ , and  $T$ , respectively.  $\hat{P}_T$  stands for the isospin projection operator onto the total isospin 0 or 1 as  $T = 0$  or  $T = 1$ , respectively. Explicitly,  $\hat{P}_{T=0} = (3 + \boldsymbol{\tau}_1 \cdot \boldsymbol{\tau}_2)/4$  and  $\hat{P}_{T=1} = (1 - \boldsymbol{\tau}_1 \cdot \boldsymbol{\tau}_2)/4$ .

The phenomenological contact amplitude,  $M_c$ , is now decomposed in terms of spin amplitudes similar to Eqs. (12) as well. Following the essential idea of Ref. [61], the corresponding contact term contributions are parameterized as

$$\begin{aligned} M_{c++} &= M_{c--} \\ &= \sum_{L,T} g_1^{LT} \left( \frac{p'}{\Lambda_S} \right)^L \exp \left( -\alpha_L^T \frac{p'^2}{\Lambda_S^2} \right) P_L(\hat{\mathbf{p}} \cdot \hat{\mathbf{p}}') \hat{P}_T, \end{aligned} \quad (13a)$$

$$\begin{aligned} M_{c+-} &= -M_{c-+} \\ &= \sum_{L,T} g_2^{LT} \left( \frac{p'}{\Lambda_S} \right)^L \exp \left( -\beta_L^T \frac{p'^2}{\Lambda_S^2} \right) P_L^1(\hat{\mathbf{p}} \cdot \hat{\mathbf{p}}') \hat{P}_T, \end{aligned} \quad (13b)$$

with  $g_1^{LT} \equiv a_L^T \exp(i\phi_a^{TL})$ ,  $g_2^{LT} \equiv b_L^T \exp(i\phi_b^{TL})$ , and  $\alpha_L^T, \beta_L^T$  being constants to be fitted.  $\phi_x^{TL}$  for  $x = a, b$  is the complex phase angle parameter which renders the contact amplitude,  $M_c$ , complex and  $\Lambda_S$  is a typical scale parameter of the reaction at hand. The momentum dependence of the partial-wave matrix elements given above is particularly well suited for hard processes, which have a large momentum transfer and whose amplitudes are expected to be independent of energy and nearly constant apart from the centrifugal barrier effects. Though reaction (1) is not a very hard process,<sup>6</sup> the  $p'^L$ -dependence

<sup>4</sup> There are in total four spin matrix elements to describe the reaction (1). However, only two of them, corresponding to the spin-non-flip and spin-flip processes, are independent due to the reflection symmetry about the reaction plane for parity conserving processes. See Ref. [55] for more detailed discussions.

<sup>5</sup> Here, the phase convention for the associated Legendre function is such that  $P_1^1(x) = \sin(x)$ .

<sup>6</sup> For example, the momentum transfer of this reaction at threshold is about 200 MeV.

nonetheless captures the essence of the behavior of the amplitude at low momentum in the final state. For further details, we refer to Ref. [61]. The exponential factor in Eq. (13) is simply a damping factor to suppress the high momentum behavior introduced by  $p'^L$ .

It should be noted that our phenomenological contact term,  $M_c$ , can only account for effects with a smooth energy dependence. Effects from, for example, dynamically generated resonances and/or channel couplings [62–65], etc., that exhibit a strong variation of the amplitude as a function of energy cannot be described by the contact term.

The amplitudes  $M_s$ ,  $M_u$ , and  $M_c$  must be added up to obtain the total scattering amplitude of Eq. (11). To ensure that there is no ambiguity in the relative phase of  $M_s + M_u$  and  $M_c$  caused by different Feynman rules, we give an explicit calculation of  $M_s$  and  $M_u$  for  $\Lambda(1116)$  in the Appendix.

Standard effective Lagrangian approaches include tree-level  $s$ -,  $u$ - and  $t$ -channel diagrams, without phenomenological contact terms. Apart from crossing symmetry demands, the inclusion of the  $u$ -channel amplitude,  $M_u$ , in particular, is necessary to reproduce the backward peaking of the differential cross sections. (See Sec. III.) In fact, there are a number of  $\Lambda$  and  $\Sigma$  resonances (cf. Table I) that may contribute to this reaction. However, it happens that the  $u$ -channel resonance contributions, especially from many of the sub-threshold resonances, also give rise to a total cross section which keeps increasing with energy in the present reaction process. This feature is not supported by the data, which reach a peak and then fall off as a function of energy. Thus, one needs a dynamical mechanism to suppress this rise in energy.

The effective Lagrangian approaches of Refs. [50, 51] have introduced phenomenological mechanisms for dealing with this problem that are very similar in spirit albeit somewhat different in technical detail. In both approaches, the rise of the  $u$ -channel resonance diagrams was suppressed with functions that smoothly cut off their contributions at high energies.<sup>7</sup> While the respective procedures generally provide satisfactory agreement with the data, they both violate crossing symmetry even at the tree-level.

In our model calculations, we also see the same undesirable rise of  $u$ -channel contributions if we leave out contact terms. We interpret this to mean that the rescattering term  $V^{\text{NP}}G_0T^{\text{NP}}$  of the non-pole  $T$ -matrix in Eq. (4) would be responsible for providing the cancellation for the increasing  $u$ -channel resonance amplitudes. We account here phenomenologically for these in detail very complex dynamics by introducing contact terms, and our results in Sec. III will show that this will indeed allow us

to treat both  $s$ - and  $u$ -channel contributions consistently, and at the same time avoid the high-energy  $u$ -channel contributions.

In general, it seems that the problem has two scales, corresponding to long-range and short-range dynamics. The latter is, of course, sensitive to the form factors used at the meson-baryon vertices to account for the composite nature of the hadrons, and the use of phenomenological contact terms seems to be warranted to account for additional structure effects. Problems with two scales have been addressed in the past, where some authors have introduced two form factors, one soft and other hard, to mimic such effects [67]. Also, in effective field theories the unknown short-range dynamics is accounted for by contact terms.

### III. RESULTS

In this section, we present our results for the reaction  $\bar{K} + N \rightarrow K + \Xi$  in different isospin channels. More specifically, we investigate the reactions  $K^- + p \rightarrow K^+ + \Xi^-$ ,  $K^- + p \rightarrow K^0 + \Xi^0$ , and  $K^- + n \rightarrow K^0 + \Xi^-$  considering all the available data on the total and differential cross sections as well as recoil polarization asymmetries.

Before we present our results, we briefly remark on the experimental data considered in this work, i.e., total cross sections, differential cross sections, and recoil polarization asymmetries. These data come from different sources [30–34, 36, 37, 40] and are available in various forms. Some of them are not in the tabular (numerical) form that can be readily used but are given only in graphical form or as parametrization in terms of the Legendre polynomial expansions. In Ref. [50], Sharov *et al.* have carefully considered the data extraction from these papers. We have checked that the extracted data are consistent with those in the original papers within the permitted accuracy of the check. In the present work, we use these data, and no cross sections resulting from the expansion coefficients are considered here.

As mentioned before, there are a number of 3- and 4-star  $\Lambda$  and  $\Sigma$  resonances, including those low-mass sub-threshold ones that contribute, in principle, to reaction (1). A list of these hyperon resonances and some of their properties is shown in Table I. However, apart from the ground state  $\Lambda(1116)$  and  $\Sigma(1193)$ , the required information for most of these resonances on the resonance parameters, such as the coupling strength (including their signs) to  $\Xi$  and/or  $N$ , are largely unknown. Therefore, the strategy adopted in this work is to consider these parameters as fit parameters and consider the minimum number of resonances required to reproduce the existing data. In particular, we have considered only those resonances that give rise to a considerable contribution to the cross section within a physically reasonable range of the resonance parameter values. More specifically, during the fitting procedure, resonances were added one by one to the model and the quality of fit was checked. It should be

<sup>7</sup> According to a private communication by one of the authors of Ref. [51], the form factor given in Eq. (3) of that work only applies to the  $s$ -channel; the  $u$ -channel was suppressed instead by the form factor given in Eq. (5) of Ref. [66].

TABLE I. The  $\Lambda$  and  $\Sigma$  hyperons listed by the Particle Data Group [17] (PDG) as three- or four-star states. The decay widths and branching ratios of higher-mass resonances ( $m_r > 1.6$  GeV) are in a broad range, and the coupling constants are determined from their centroid values. In the present work, the masses ( $m_r$ ) and widths ( $\Gamma_r$ ) of the hyperons as given in this table have been used, except for the  $\Sigma(2250)$  resonance. For the latter resonance, see the text.

$\Lambda$ states					$\Sigma$ states				
State	$m_r$ (MeV)	$\Gamma_r$ (MeV)	Rating	$ g_{NAK} $	State	$m_r$ (MeV)	$\Gamma_r$ (MeV)	Rating	$ g_{N\Sigma K} $
$\Lambda(1116)$ $1/2^+$	1115.7		****		$\Sigma(1193)$ $1/2^+$	1193		****	
$\Lambda(1405)$ $1/2^-$	1406	50	****		$\Sigma(1385)$ $3/2^+$	1385	37	****	
$\Lambda(1520)$ $3/2^-$	1520	16	****						
$\Lambda(1600)$ $1/2^+$	1600	150	***	4.2	$\Sigma(1660)$ $1/2^+$	1660	100	***	2.5
$\Lambda(1670)$ $1/2^-$	1670	35	****	0.3	$\Sigma(1670)$ $3/2^-$	1670	60	****	2.8
$\Lambda(1690)$ $3/2^-$	1690	60	****	4.0	$\Sigma(1750)$ $1/2^-$	1750	90	***	0.5
$\Lambda(1800)$ $1/2^-$	1800	300	***	1.0	$\Sigma(1775)$ $5/2^-$	1775	120	****	
$\Lambda(1810)$ $1/2^+$	1810	150	***	2.8	$\Sigma(1915)$ $5/2^+$	1915	120	****	
$\Lambda(1820)$ $5/2^+$	1820	80	****		$\Sigma(1940)$ $3/2^-$	1940	220	***	< 2.8
$\Lambda(1830)$ $5/2^-$	1830	95	****		$\Sigma(2030)$ $7/2^+$	2030	180	****	
$\Lambda(1890)$ $3/2^+$	1890	100	****	0.8	$\Sigma(2250)$ $?^?$	2250	100	***	
$\Lambda(2100)$ $7/2^-$	2100	200	****						
$\Lambda(2110)$ $5/2^+$	2110	200	***						
$\Lambda(2350)$ $9/2^+$	2350	150	***						

mentioned that we have also checked the influence of various combinations of resonances at a time (and not just one by one) to the fit quality. The resonances kept in the presented calculation were those that increased the quality of the fit by a noticeable amount with the variation in  $\chi^2$  per data points  $N$ , namely,  $\delta\chi^2/N > 0.1$ . An example of this procedure is shown in Table II where the results of adding one more resonance to the current model, as specified later, is shown. We see that some of these resonances improve the fit quality of the total cross section but not the other observables or even worsen the fit quality slightly. We have not included these resonances into our model because the total cross sections suffer from relatively large uncertainties.

Whenever appropriate, for each resonance considered in this work, the corresponding coupling constants  $g_{KYN}$  and  $g_{KY\Xi}$  were constrained in such way that the sum of the branching ratios  $\beta_{Y \rightarrow KN} + \beta_{Y \rightarrow K\Xi}$  not to exceed unity. Because, within our model, the data are sensitive only to the product of the coupling constants  $g_{KYN}g_{KY\Xi}$ , setting  $|g_{KYN}| = |g_{KY\Xi}|$  for the purpose of estimating the individual branching ratios, and only for this purpose, is a simple way of keeping our coupling constant values within a physically acceptable range. Admittedly, the currently existing data are limited and suffer from large uncertainties, thus an accurate determination of the resonance parameters are not possible at this stage. For this, one needs to wait for new more precise data, possibly including more spin polarization data. In this regard, the multi-strangeness baryon spectroscopy program using the antikaon beam at J-PARC will be of particular relevance. For the ground states  $\Lambda(1116)$  and  $\Sigma(1193)$ , the corresponding coupling constants are estimated based on the flavor SU(3) symmetry relations [23].

It should be mentioned that, in principle, the coupling constants  $g_{KYN}$  and  $g_{KY\Xi}$  are complex quantities ow-

ing to the dressing mechanism of the resonance vertex as given by Eq. (8). In the present work, we restrict them to be pure real to reduce the number of free parameters and for the sake of simplicity. Note that the complex phases of the coupling constants are not arbitrary in that they are constrained by unitarity of the scattering amplitude [68], a feature that is absent in the amplitude based on a tree-level approximation as mentioned in the introduction. However, we found that fit quality was not improved when we ignored theoretical constraints and simply allowed for complex phases in the coupling constants. A simple and proper way of accounting for unitarity within an effective Lagrangian approach, such as the present one, is being developed and will soon be available elsewhere [69].

The phenomenological contact amplitude  $M_c$  contains two sets of free parameters,  $\{g_1^{LT}, \alpha_L^T\}$  and  $\{g_2^{LT}, \beta_L^T\}$ , to be fixed by adjusting to reproduce the experimental data, for a given set of  $\{L, T\}$  as shown in Eq. (13). In order to reduce the number of free parameters, we have assumed the parameter  $\alpha_L^T$  to be equal to  $\beta_L^T$  and independent on  $T$  and  $L$ , i.e.,  $\alpha_L^T = \beta_L^T = \alpha$ . The scale parameter  $\Lambda_S$  has been fixed as  $\Lambda_S = 1$  GeV. Note that the phenomenological contact amplitude can and should be complex in principle, since it accounts for the rescattering contribution ( $V^{\text{NP}}GT^{\text{NP}}$ ) of the non-pole  $T$ -matrix which is complex in general. Accordingly, the coupling strength parameters  $g_1^{LT}$  and  $g_2^{LT}$  are complex quantities. In order to reduce the number of free parameters, we take their phases to be independent on  $L$  and  $T$ , so that,  $\phi_a^{TL} = \phi_a$  and  $\phi_b^{TL} = \phi_b$  for all sets  $\{L, T\}$ . Also, in the present calculation, we find that it suffices to consider partial waves up to  $L = 2$  in the contact amplitude to reproduce the existing data.

The resonances included in the present model calculations and the corresponding resonance parameters are

TABLE II. Variation in  $\chi^2$  per data point  $N$ ,  $\delta\chi^2/N$ , obtained when adding one more resonance to the current model (specified in Table. III). A negative  $\delta\chi^2/N$  corresponds to an improvement in the result. The quantity  $\delta\chi_i^2/N_i$  corresponds to  $\delta\chi^2/N$  evaluated for a given type of observable specified by index  $i = \sigma$ (total cross section),  $d\sigma$ (differential cross section), and  $P$ (recoil asymmetry).  $N = N_\sigma + N_{d\sigma} + N_P$  denotes the total number of data points. Furthermore,  $\delta\chi_i^2/N_i$  is given for the charged  $\Xi^-$  ( $\delta\chi_-^2/N_-$ ) and neutral  $\Xi^0$  ( $\delta\chi_0^2/N_0$ ) production processes, separately. The last column corresponds to  $\delta\chi^2/N$  of the global fit considering all the data of both reaction processes. The last row corresponds to  $\chi_i^2/N_i$  of the current model.

Y added	$K^- + p \rightarrow K^+ + \Xi^-$				$K^- + p \rightarrow K^0 + \Xi^0$				$\delta\chi^2/N$
	$\delta\chi_\sigma^2/N_\sigma$	$\delta\chi_{d\sigma}^2/N_{d\sigma}$	$\delta\chi_P^2/N_P$	$\delta\chi_-^2/N_-$	$\delta\chi_\sigma^2/N_\sigma$	$\delta\chi_{d\sigma}^2/N_{d\sigma}$	$\delta\chi_P^2/N_P$	$\delta\chi_0^2/N_0$	
$\Lambda(1405)$	-0.01	0.03	0.00	-0.01	0.03	0.00	0.02	0.01	0.00
$\Lambda(1600)$	-0.02	0.00	-0.01	-0.01	0.02	0.00	0.02	0.01	0.00
$\Lambda(1670)$	-0.01	0.00	0.00	0.00	0.02	0.00	0.02	0.01	0.00
$\Lambda(1800)$	0.00	0.01	0.00	0.00	-0.01	0.00	0.01	0.00	0.00
$\Lambda(1810)$	-0.01	-0.01	0.00	-0.01	0.02	0.00	0.02	0.01	0.00
$\Lambda(1520)$	-0.06	0.02	0.00	0.00	-0.05	-0.01	0.00	-0.02	0.00
$\Lambda(1690)$	0.00	0.00	0.00	0.00	0.00	0.00	0.00	0.00	0.00
$\Lambda(1820)$	-0.08	0.01	0.01	0.00	-0.07	0.00	-0.02	-0.02	-0.01
$\Lambda(1830)$	-0.05	0.01	0.01	0.00	0.00	0.02	0.02	0.01	0.00
$\Lambda(2110)$	-0.02	0.02	0.01	0.01	-0.03	-0.01	-0.03	-0.02	0.00
$\Lambda(2100)$	-0.08	0.04	0.03	0.02	-0.04	-0.02	-0.01	-0.03	0.01
$\Sigma(1660)$	-0.02	0.00	0.00	0.00	-0.01	0.01	0.00	0.01	0.00
$\Sigma(1750)$	-0.01	0.01	0.00	0.00	-0.01	0.01	0.00	0.00	0.00
$\Sigma(1670)$	-0.01	0.00	-0.01	0.00	0.02	0.01	0.01	0.01	0.00
$\Sigma(1940)$	0.02	0.00	0.01	0.00	0.01	-0.01	0.01	-0.01	0.00
$\Sigma(1775)$	-0.01	0.01	0.04	0.01	-0.02	0.00	-0.02	-0.01	0.00
$\Sigma(1915)$	0.01	-0.01	0.00	-0.01	-0.03	0.00	0.00	-0.01	-0.01
	$\chi_\sigma^2/N_\sigma$	$\chi_{d\sigma}^2/N_{d\sigma}$	$\chi_P^2/N_P$	$\chi_-^2/N_-$	$\chi_\sigma^2/N_\sigma$	$\chi_{d\sigma}^2/N_{d\sigma}$	$\chi_P^2/N_P$	$\chi_0^2/N_0$	$\chi^2/N$
	1.53	1.64	1.89	1.65	0.88	1.06	1.74	1.10	1.49

TABLE III. Fitted parameter values of the current model. For the details of the resonance parameters, see the Appendix. For the contact amplitude, see Eq. (13). The entries in boldface are taken from Ref. [23] and they are not fit parameters. Here, it is assumed that  $\phi_a^{TL} = \phi_a$  and  $\phi_b^{TL} = \phi_b$ , in addition to  $\alpha_L^T = \beta_L^T = \alpha$ .

Y	$g_{NAK}$	$\lambda_{NAK}$	$g_{\Xi AK}$	$\lambda_{\Xi AK}$	$\Lambda$ (MeV)							
$\Lambda(1116)_{\frac{1}{2}^+}$	-13.24	1.0	3.52	1.0	900							
$\Sigma(1193)_{\frac{1}{2}^+}$	3.58	1.0	-13.26	1.0	900							
	$g_{NAK}g_{\Xi AK}$	-	-	-	$\Lambda$ (MeV)	$L$	$a_L^0$	$a_L^1$	$b_L^0$	$b_L^1$	$\phi_a$	$\phi_b$
$\Lambda(1890)_{\frac{3}{2}^+}$	0.11				900	0	0.28	-1.19				
$\Sigma(1385)_{\frac{3}{2}^+}$	18.76				900	1	3.23	-4.84	-3.40	0.61		
$\Sigma(2030)_{\frac{7}{2}^+}$	0.49				900	2	3.06	21.07	9.40	-2.28		
$\Sigma(2250)_{\frac{5}{2}^-}$	-0.033				900		$\Lambda_S = 1$ GeV		$\alpha = 3.60$	0.22	-0.16	

displayed in Table III as well as the parameters of the phenomenological contact term,  $M_c$ . We do not give the associated uncertainties here because they are not well constrained. In the present calculation, resonances with  $J \leq 7/2$  were considered. The masses and the total widths of the resonances are taken to be those quoted in PDG [17] and are given in Table I, except for the mass of the  $\Sigma(2250)$  resonance. Currently, the  $\Sigma(2250)$  resonance is not well established and has a three-star status [17]. In fact, the PDG does not even assign the spin-parity quantum numbers for this resonance. The analyses of Ref. [39] provide two possible parameter sets, one with  $J^P = 5/2^-$  at about  $2270 \pm 50$  MeV and another with  $J^P = 9/2^-$  at about  $2210 \pm 30$  MeV. In the present work we have assumed  $\Sigma(2250)$  to have  $J^P = 5/2^-$  with the mass of 2265 MeV, the primary reason being that the total cross section in  $K^- + p \rightarrow K^+ + \Xi^-$  shows a small

bump structure at around 2300 MeV, which is well reproduced in our model with these parameter values. For the corresponding width, we have adopted the value quoted in PDG as shown in Table I.

All parameters of the present model calculation are determined as described above and we now present the results obtained from our model. The overall fit quality is quite good with  $\chi^2/\text{d.o.f.} = 1.55$  or  $\chi^2/N = 1.49$ , as displayed in Table II. There, we also show the partial  $\chi$ -squared values  $\chi_i^2/N_i$  evaluated for a given type of observable specified by the index  $i$  as explained in the caption of Table II. In Fig. 2 we show the results for the total cross section in the charged  $\Xi$  production reaction from the proton target,  $K^- + p \rightarrow K^+ + \Xi^-$ , for the c.m. energies up to  $W = 3$  GeV. Figure 2(a) displays the total contribution, which reproduces the data rather well. The dynamical content of the present model is also

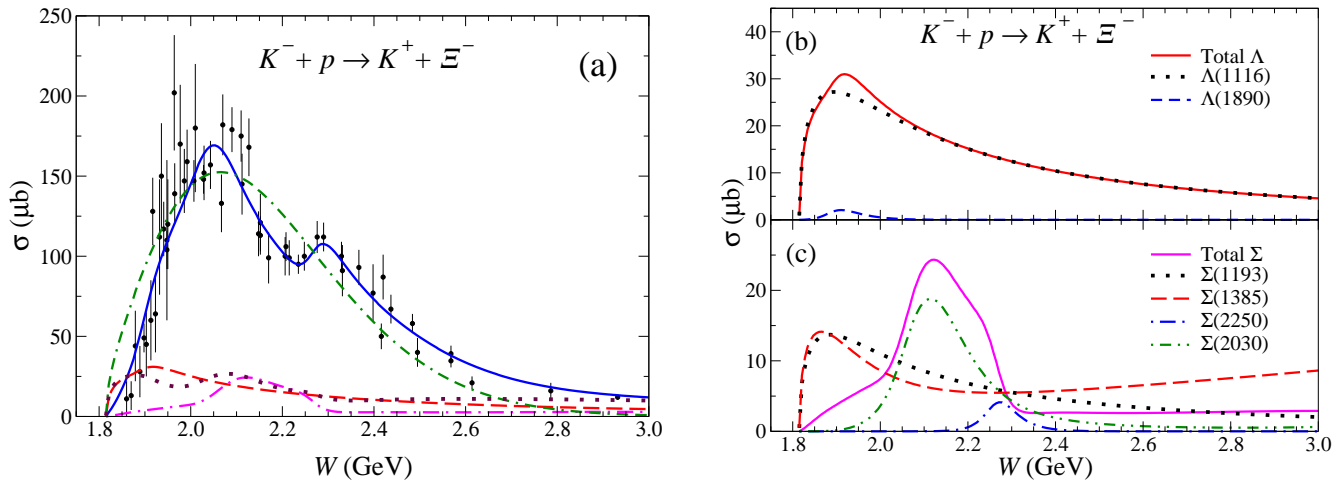


FIG. 2. (Color online) Total cross section for the  $K^- + p \rightarrow K^+ + \Xi^-$  reaction. (a) The solid blue line represents the result of the full calculation of the present model. The red dashed line shows the combined  $\Lambda$  hyperons contribution. The magenta dash-dotted line shows the combined  $\Sigma$  hyperons contribution. The brown dotted line shows the combined  $\Lambda$  and  $\Sigma$  hyperons contribution. The green dash-dash-dotted line corresponds to the contact term. (b) The solid red line represents the combined  $\Lambda$  hyperons contribution that is the same as the red dashed line in (a). The dotted and dashed lines show the  $\Lambda(1116)$  and  $\Lambda(1890)$  contributions, respectively. (c) The solid magenta line represents the combined  $\Sigma$  hyperons contribution that is the same as the magenta dash-dotted line in (a). The dotted, dashed, dot-dashed, and dot-dot-dashed lines show the contributions from the  $\Sigma(1193)$ ,  $\Sigma(1385)$ ,  $\Sigma(2250)$ , and  $\Sigma(2030)$ , respectively. The experimental data (black circles) are the digitized version as quoted in Ref. [50] from the original work of Refs. [29–34, 36–39, 41–43].

shown in the same figure. We find that the contact term rises quickly from threshold peaking at around 2.1 GeV and falls off slowly as energy increases. It dominates the cross section except for energies very close to threshold and above  $\sim 2.7$  GeV, where the hyperon resonance contributions are comparable. The  $\Lambda$  hyperons contribution is strongest near threshold and falls off very slowly as energy increases. The  $\Sigma$  hyperons contribution is relatively small over the entire energy range considered, except in the interval of 2.0–2.3 GeV, where it becomes comparable to the  $\Lambda$  contribution. Near threshold, there is a strong destructive interference between the contact term and (mainly) the  $\Lambda$  hyperons contribution. At higher energies, the data indicates an existence of a bump structure at  $W \sim 2.3$  GeV. Our model reproduces this feature via delicate destructive and constructive interferences of the contact term and the hyperon resonance contributions. We also mention that we have explored the possibility of a much smaller contact amplitude contribution than shown in Fig. 2(a) considering various different sets of hyperon resonances from Table I; however, we were unable to find a solution with a fit quality comparable to that of Fig. 2(a).

Figure 2(b) displays the individual  $\Lambda$  hyperon contributions. We see that the ground state  $\Lambda(1116)$  is, by far, the dominant contribution which is due to the tail of the corresponding  $u$ -channel process. Analogously, the individual  $\Sigma$  hyperon contributions are shown in Fig. 2(c). Here, the relatively small cross section near threshold is due to the destructive interference between the  $\Sigma(1192)$  and  $\Sigma(1385)$ . The enhancement of the cross section in

the energy interval of 2.0–2.3 GeV is mostly due to the  $\Sigma(2030)$  resonance. The  $\Sigma(2250)$  leads to a little shoulder in the total  $\Sigma$  contribution. We note that any non-negligible contribution from the hyperons for energies above  $\sim 2.3$  GeV is due to the  $u$ -channel processes.

In Fig. 3, we show the total cross section results for the neutral  $\Xi$  production process,  $K^- + p \rightarrow K^0 + \Xi^0$ . Here, the data are of such poor quality that they impose much less constraint on the model parameters than the corresponding data in the charged  $\Xi^-$  production. The resulting dynamical content shown in Fig. 3(a) is similar to that for the charged  $\Xi^-$  production discussed above, i.e., it is largely dominated by the contact term. However, we see a quite different feature in the  $\Lambda$  and  $\Sigma$  resonance contributions as compared to that for the charged  $\Xi^-$  production [cf. Fig. 2(a)]. One notable difference between the charged and neutral  $\Xi$  production reactions considered here is that the  $u$ -channel  $\Lambda$  hyperon contribution is absent in the  $\Xi^0$  production case. Also, the relative contribution of the  $\Sigma$  hyperons is much larger in the neutral  $\Xi^0$  production than in the charged  $\Xi^-$  production, especially, in the near threshold region.

Figures 3(b) and 3(c) show the individual hyperon contributions. As mentioned before, due to the absence of the  $u$ -channel  $\Lambda$  exchange in the neutral  $\Xi^0$  production, the  $\Lambda(1116)$  contribution is insignificant, leading to a negligible contribution of the  $\Lambda$  hyperons. Due to the isospin factors here, the  $\Sigma(1192)$  and  $\Sigma(1385)$  hyperons interfere constructively, especially near the threshold. Recall that, for charged  $\Xi^-$  production, these hyperons interfere destructively [cf. Fig. 2(c)].



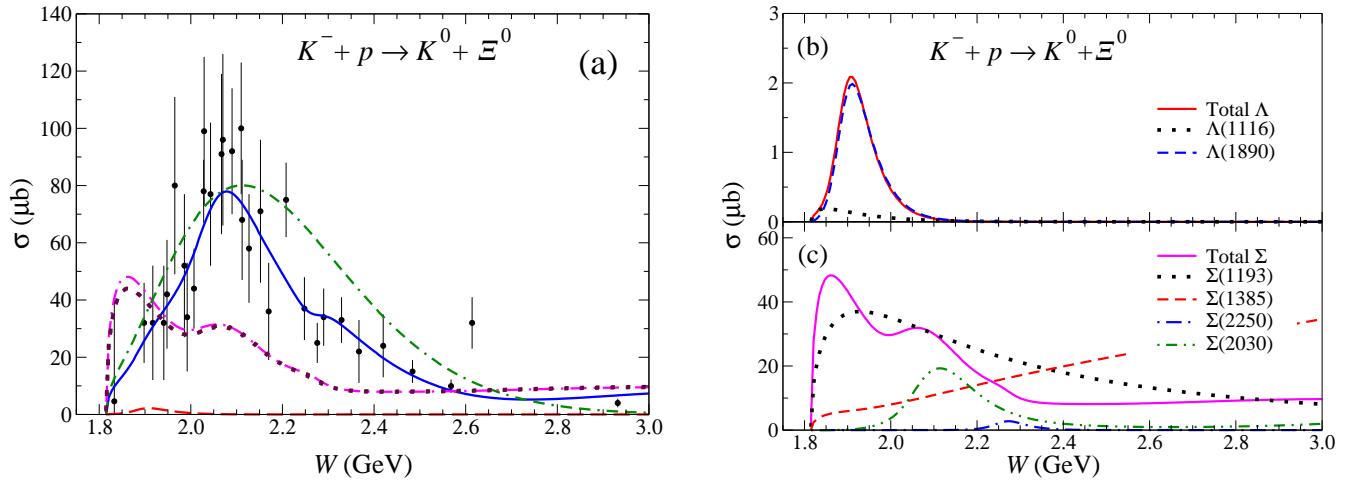


FIG. 3. (Color online) Same as Fig. 2 for the  $K^- + p \rightarrow K^0 + \Xi^0$  reaction. The experimental data (black circles) are the digitized version as quoted in Ref. [50] from the original work of Refs. [30, 37–40, 43].

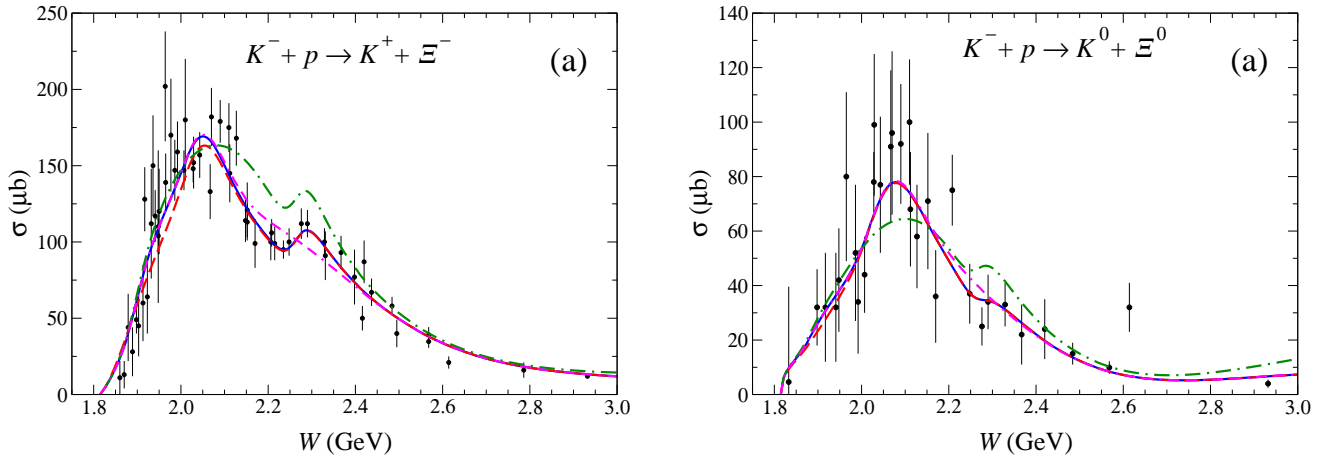


FIG. 4. (Color online) Total cross section results with individual resonances switched off (a) for  $K^- + p \rightarrow K^+ + \Xi^-$  and (b) for  $K^- + p \rightarrow K^0 + \Xi^0$ . The blue lines represent the full result shown in Figs. 2 and 3. The red dashed lines, which almost coincide with the blue lines represent the result with  $\Lambda(1890)$  switched off. The green dash-dotted lines represent the result with  $\Sigma(2030)$  switched off and the magenta dash-dash-dotted lines represent the result with  $\Sigma(2250)5/2^-$  switched off.

In Fig. 4 we illustrate the amount of the above-threshold resonance contributions of the present model to the total cross sections. We do this by comparing the full results shown in Figs. 2(a) and 3(a) to the result found by switching off one resonance at a time. We see in Fig. 4(a) that the largest effect of  $\Sigma(2030)$  on the cross sections is in the range of  $W \sim 2.0$  to  $2.4$  GeV. This resonance is clearly needed in our model to reproduce the data. It also affects the recoil polarization as will be discussed later. It should be mentioned that this resonance also helps to reproduce the measured  $K^+\Xi^-$  invariant mass distribution in  $\gamma + p \rightarrow K^+ + K^+ + \Xi^-$  [24], by filling in the valley between the two bumps in the invariant mass distribution that would appear without it; such a feature clearly is not observed in the data [19]. The  $\Lambda(1890)$  affects the total cross section in the range of  $W \sim 1.9$  to  $2.1$  GeV, and the  $\Sigma(2250)5/2^-$  contributes

around  $W \sim 2.2$  GeV, where it is needed to reproduce the observed bump structure. A more accurate data set is clearly needed for a more definitive answer about the roles of the  $\Lambda(1890)$  and  $\Sigma(2250)$  resonances. Figure 4(b), for the neutral  $\Xi^0$  production, also shows a similar feature observed in the  $\Xi^-$  case for the  $\Sigma(2030)$  resonance. Here, the influence of the  $\Sigma(2250)5/2^-$  is smaller and that of the  $\Lambda(1890)$  is hardly seen. Recall that there is no  $u$ -channel  $\Lambda$  contribution in the neutral  $\Xi^0$  production.

The results for differential cross sections in both  $K^- + p \rightarrow K^+ + \Xi^-$  and  $K^- + p \rightarrow K^0 + \Xi^0$  are shown in Figs. 5(a) and 5(b), respectively, in the energy domain up to  $W = 2.8$  GeV for the former and up to  $W = 2.5$  GeV for the latter reaction. Overall, the model reproduces the data quite well. As in the total cross sections, the data for the neutral  $\Xi^0$  production are fewer and less accurate

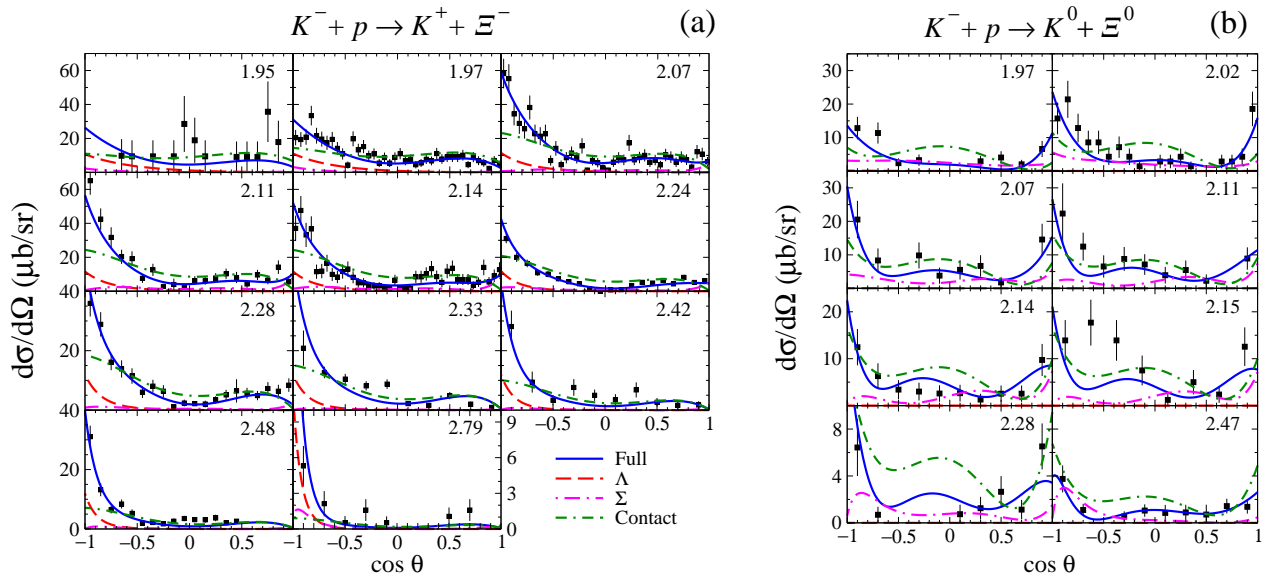


FIG. 5. (Color online) Kaon angular distributions in the center-of-mass frame (a) for  $K^- + p \rightarrow K^+ + \Xi^-$  and (b) for  $K^- + p \rightarrow K^0 + \Xi^0$ . The blue lines represent the full model results. The red dashed lines show the combined  $\Lambda$  hyperons contribution. The magenta dash-dotted lines show the combined  $\Sigma$  hyperons contribution. The green dash-dash-dotted line corresponds to the contact term. The numbers in the upper right corners correspond to the centroid total energy of the system  $W$ . Note the different scales used. The experimental data (black circles) are the digitized version as quoted in Ref. [50] from the original work of Refs. [31–34, 36, 37] for the  $K^- + p \rightarrow K^+ + \Xi^-$  reaction and of Ref. [30, 36, 37, 40] for the  $K^- + p \rightarrow K^0 + \Xi^0$  reaction.

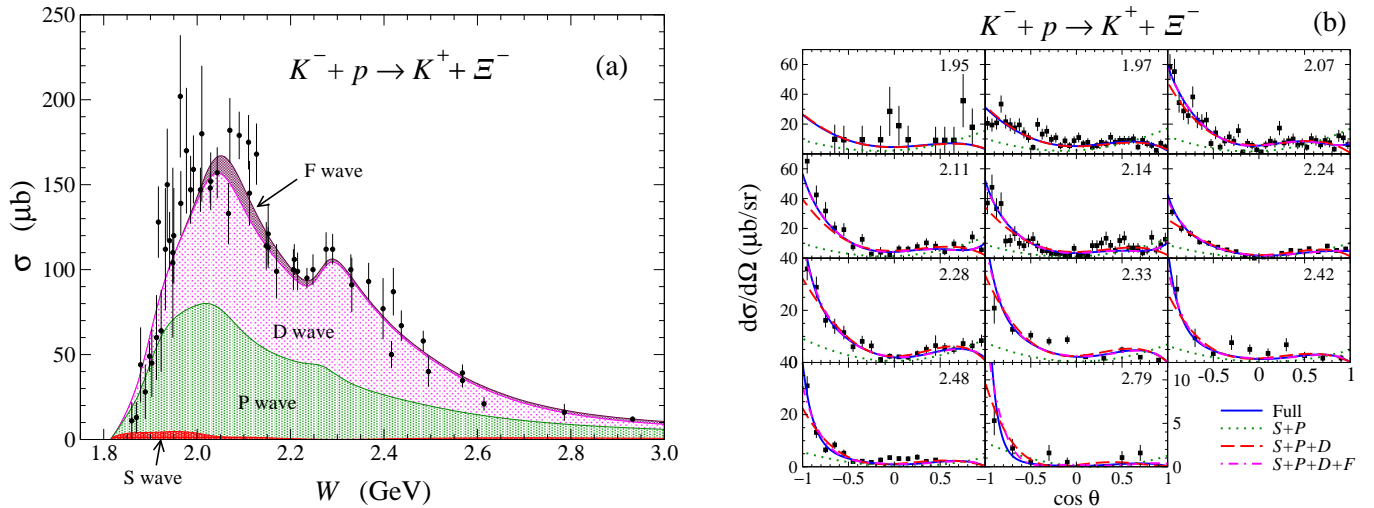


FIG. 6. (Color online) Partial wave decomposition of the total cross section and the angular distribution for  $K^- + p \rightarrow K^+ + \Xi^-$ . (a) Total cross section sectioned by contributions from each partial wave  $L$ . The red shaded area indicates the  $S$ -wave contribution, while the green area corresponds to the  $P$ -wave. Magenta indicates the  $D$ -wave and maroon the  $F$ -wave. (b)  $K^+$  angular distribution: the solid blue lines are the full results, while the dotted green lines represent the sum of  $S + P$  waves, the red dashed lines represent the  $S + P + D$  waves and the dash-dotted magenta lines represent the  $S + P + D + F$  waves. For lower energies, the  $S + P + D$  waves already saturate the full cross section results so that the  $F$ - and higher-wave contributions cannot be distinguished from the full result.

than for the charged  $\Xi^-$  production. In particular, the  $\Xi^0$  production data at  $W = 2.15$  GeV seems incompatible with those at nearby energies, and the present model is unable to reproduce the observed shape at backward angles. It is clear from Figs. 5(a) and 5(b) that the charged

channel shows a backward peaked angular distributions, while the neutral channel shows enhancement for both backward and forward scattering angles (more symmetric around  $\cos \theta = 0$ ) for all but perhaps the highest energies. In the charged  $\Xi^-$  production, both the resonance

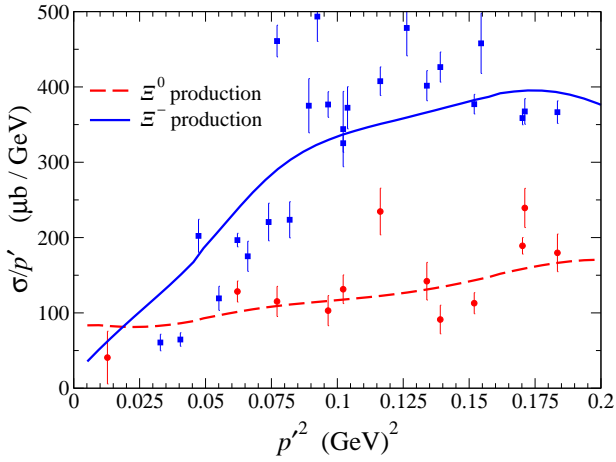


FIG. 7. (Color online) Ratio of the measured total cross section  $\sigma$  and the final state  $K\Xi$  relative momentum  $p'$  as a function of  $p'^2$ . The blue square data correspond to  $K^- + p \rightarrow K^+ + \Xi^-$ , while the red circle data to  $K^- + p \rightarrow K^0 + \Xi^0$ . The blue solid and red dashed curves are the present model results corresponding to  $K^- + p \rightarrow K^+ + \Xi^-$  and  $K^- + p \rightarrow K^0 + \Xi^0$ , respectively.

and contact amplitude contributions are backward angle peaked and, as the energy increases, they get smaller and smaller at forward angles. In  $\Xi^0$  production, both the  $\Sigma$  resonance and contact amplitude contributions also exhibit an enhancement for forward angles. Note that the  $\Lambda$  resonance contribution here is negligible due to the absence of the  $u$ -channel process. The interference pattern in the forward angular region depends on energy. At lower energies the interference is constructive and it becomes destructive at higher energies. The behavior of the angular distributions in terms of the partial waves will be discussed later in connection with the results of Figs. 6(b) and 8(b).

The partial-wave content of the cross sections for the charged  $\Xi^-$  production process arising from the present model is shown in Figs. 6(a) and 6(b). As can be seen in Fig. 6(a), the total cross section is dominated by the  $P$  and  $D$  waves in almost the entire energy range considered, even at energies very close to threshold where one sees a strongly rising  $P$ -wave contribution. The  $S$ -wave contribution is very small. This peculiar feature is caused by the ground state  $\Lambda(1116)$ , whose contribution cancels to a large extent the otherwise dominant  $S$ -wave contribution close to threshold, in addition to enhancing the  $P$ -wave contribution. One way of probing the  $S$ -wave content close to threshold in a model-independent manner is to look at the quantity  $\sigma/p'$  as a function of  $p'^2$ , where  $p'$  is the relative momentum of the final  $K\Xi$  state. The reason being that, for hard processes, the partial-wave reaction amplitude behaves basically like  $p'^L$  for a given orbital angular momentum  $L$  as mentioned in Sec. II. This leads to

$$\frac{\sigma}{p'} = c_0 + c_1 p'^2 + c_2 p'^4 + \dots, \quad (14)$$

with expansion constants  $c_L$ . Figure 7 illustrates this point. Although the existing experimental data are of poor quality, they reveal the general features just mentioned. In particular, for the charged  $\Xi^-$  production process, the data indicate a linear behavior of  $\sigma/p'$  close to threshold implying a strong  $P$ -wave contribution. Our present model result is consistent with this behavior. It is also consistent with the observation made in Ref. [53] that the low-energy behavior of the total cross sections in the  $\pi N$ ,  $\eta N$  and  $K\Xi$  channels does not seem to follow the usual  $S$ -wave dominance.

The corresponding results for the neutral  $\Xi^0$  production are also shown in Fig. 7. There, the scattered data are consistent with  $S$ -wave dominance, a feature exhibited by our model as well [see also Fig. 8(a)]. In Fig. 6(a), we also see a small  $F$ -wave contribution above  $W \sim 2.0$  GeV that helps saturate the total cross section. Note that since our contact term includes partial waves only up to  $L \leq 2$ , the  $F$ -wave contribution is entirely due to the hyperon resonances. The enhancement of the  $D$ -wave contribution around  $W = 2.3$  GeV as well as the little shoulder in the  $P$ -wave contribution are due to the  $\Sigma(2250)$  hyperon. Of course, the partial-wave contributions are mainly constrained by the differential cross section and they are shown in Fig. 6(b). As mentioned before, the shape of the angular distribution is backward-angle peaked and the cross sections are very small at forward angles. This behavior is a direct consequence of the very significant interference between the  $P$  and  $D$  waves. This can be seen by expanding the cross section in partial waves. Considering the partial waves through  $L = 2$  and following Ref. [55], the differential cross section may be expressed as

$$\begin{aligned} \frac{d\sigma}{d\Omega} = & |\alpha_{02}|^2 + \left[ |\alpha_1|^2 + 2 \operatorname{Re}(\alpha_{02} \tilde{\alpha}_2^*) \right] \cos^2 \theta \\ & + |\tilde{\alpha}_2|^2 \cos^4 \theta + \left( |\beta_1|^2 + |\tilde{\beta}_2|^2 \cos^2 \theta \right) \sin^2 \theta \\ & + 2 \operatorname{Re} \left[ \alpha_{02} \alpha_1^* + \alpha_1 \tilde{\alpha}_2^* \cos^2 \theta + \beta_1 \tilde{\beta}_2^* \sin^2 \theta \right] \cos \theta, \end{aligned} \quad (15)$$

where the coefficients  $\alpha_L$  ( $\beta_L$ ) provide a linear combination of the partial-wave matrix elements corresponding to the spin-non-flip (spin-flip) process with a given orbital angular momentum  $L$  [see Eq. (12)]. Here,  $\alpha_{02} \equiv \alpha_0 - \frac{1}{3} \tilde{\alpha}_2$ ,  $\tilde{\alpha}_2 \equiv \frac{2}{3} \alpha_2$ , and  $\tilde{\beta}_2 \equiv 3\beta_2$ . In the above equation, the last term on the right-hand side involving an interference between the  $P$  and  $D$  waves is an odd function in  $\cos \theta$ , while the the first term in square brackets is an even function. These two terms cancel to a large extent at forward angles while at backward angles they add up. Note that these partial waves are comparable in strength as shown in Fig. 6(a) so that their interference term leading to an odd function part can largely cancel the even term at forward angles.

Figures 8(a) and 8(b) display the partial wave content in the cross sections for the neutral  $\Xi^0$  production process. In contrast to the charged  $\Xi^-$  production, here

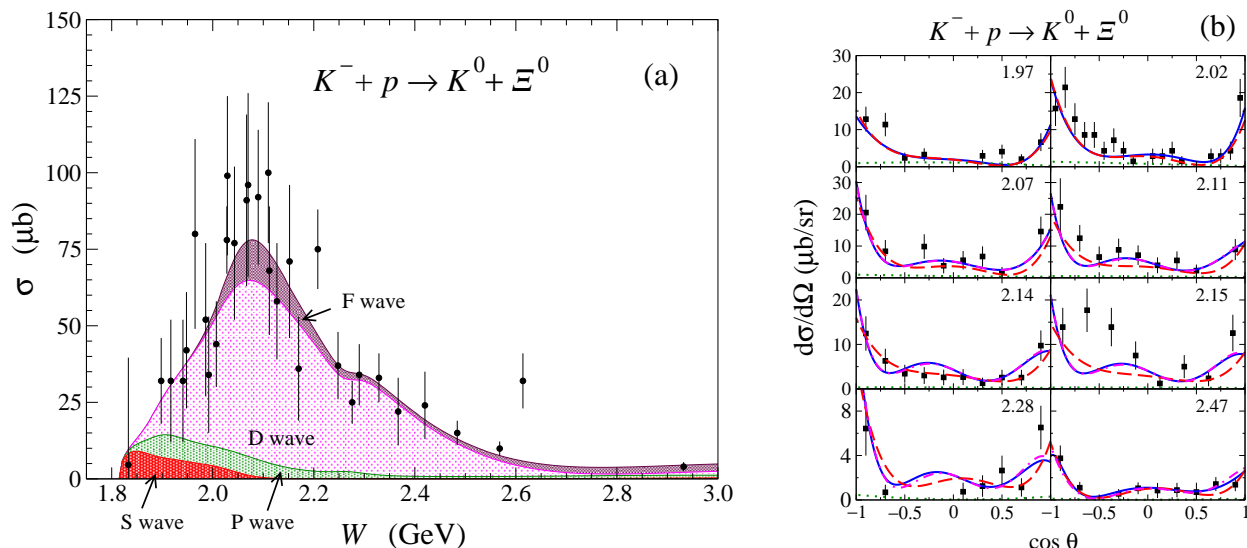


FIG. 8. (Color online) Same as in Fig. 6 but for  $K^- + p \rightarrow K^0 + \Xi^0$ .

one sees that the largest contribution to the total cross section is the  $D$ -wave, and the  $P$ -wave is largely suppressed, which is a direct consequence of the shape of the observed angular distribution whose partial wave contributions are shown in Fig. 8(b). There, compared to that for charged  $\Xi^-$ , one sees a more symmetric angular shape about  $\cos\theta = 0$  that is dominated by the  $D$ -wave. The present model reproduces the observed behavior of the  $K^0$  angular distribution by suppressing the  $P$ -wave contribution as can be easily understood from Eq. (15). The rather drastic suppression of the  $P$  wave can be better seen in Fig. 8(a). For energies very close to threshold, the cross section is dominated by the  $S$ -wave as seen also in Fig. 8(a).

The results for the recoil polarization asymmetry multiplied by the cross section are shown in Fig. 9 in the energy interval of  $W = 2.1$  to  $2.5$  GeV. Overall, we reproduce the data reasonably well. We also find that the results shown at  $W = 2.11$  GeV are still significantly affected by  $\Sigma(2030)$ . This corroborates the findings of Ref. [50]. We recall that the recoil asymmetry is proportional to the imaginary part of the product of the non-spin-flip matrix element ( $M_{ss}$ ) with the complex conjugate of the spin-flip matrix element ( $M_{s's}$  with  $s' \neq s$ ) [55], so that it vanishes identically unless these matrix elements are such that their product has a non-vanishing imaginary part. We can therefore expect the recoil polarization to be sensitive to the complex nature of the reaction amplitude, in particular, to the phenomenological contact amplitude,  $M_C$ , introduced in the present model. Indeed, if one forces the coupling strength parameters,  $g_1^{LT}$  and  $g_2^{LT}$  in Eq. (13), to be pure real during the fitting procedure, the  $\chi_P^2/N_P$  deteriorates, e.g., from 1.89 to 2.26 for the  $K^- + p \rightarrow K^+ + \Xi^-$  reaction, although the quality of fit for cross sections is nearly unchanged.

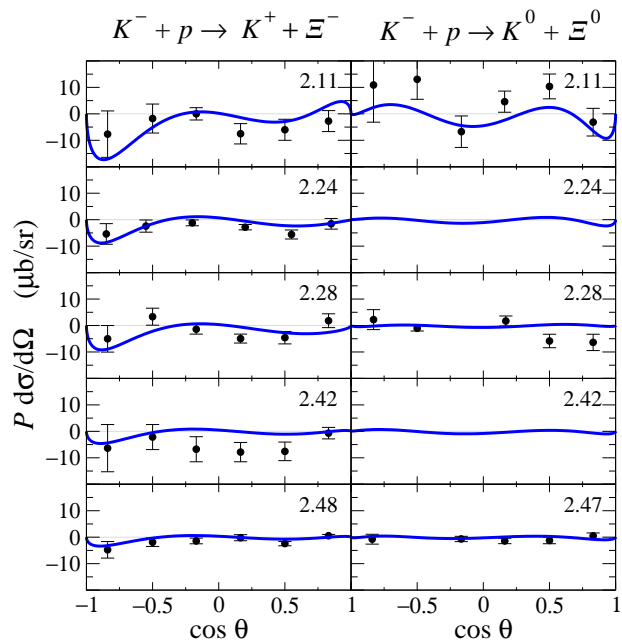


FIG. 9. (Color online) The recoil asymmetry multiplied by the cross section,  $P \frac{d\sigma}{d\Omega}$ , for both the  $K^- + p \rightarrow K^+ + \Xi^-$  and  $K^- + p \rightarrow K^0 + \Xi^0$  reactions. The blue solid lines represent the full results of the current model. Data are from Refs. [33, 37].

In Fig. 10, we show the present model predictions for the target-beam asymmetries,  $K_{xx}$  and  $K_{xz}$ , multiplied by the unpolarized cross section, i.e.,  $\frac{d\sigma}{d\Omega} K_{xx}$  and  $\frac{d\sigma}{d\Omega} K_{xz}$  for both the charged  $\Xi^-$  and neutral  $\Xi^0$  production processes. These observables are related to the spin-rotation parameter  $\beta$  [70] by  $\tan\beta = -K_{xz}/K_{xx}$ . Note that these target-recoil asymmetries, together with  $K_{yy}$ , are the only three independent double-spin observables in the reaction of Eq. (1) as discussed in Ref. [55]. Indeed, the

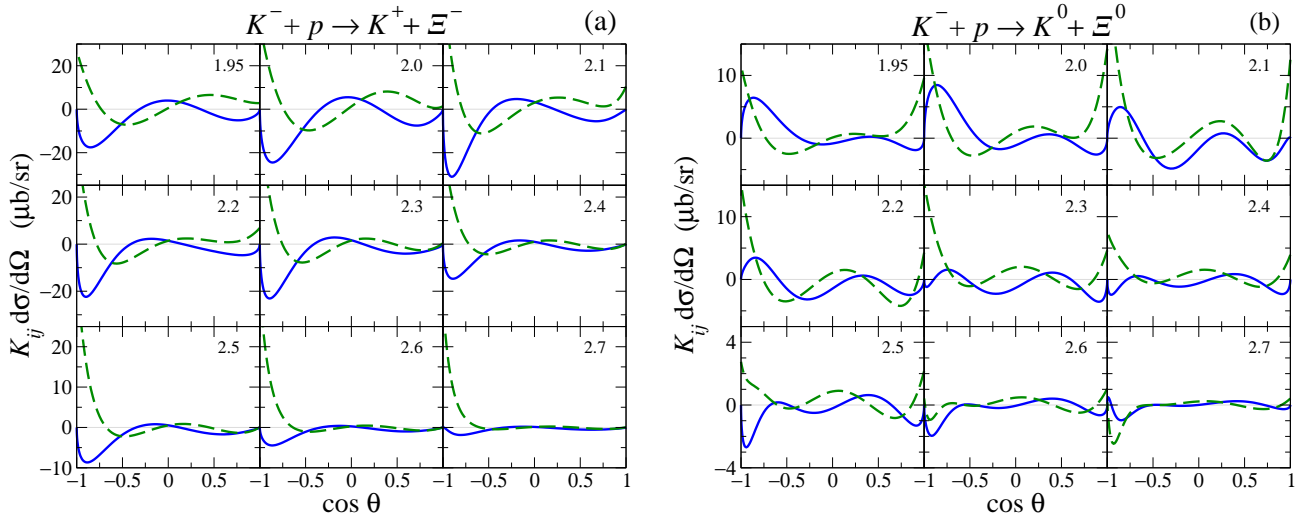


FIG. 10. (Color online) Target-recoil asymmetries  $K_{xx}$  (green dashed curves) and  $K_{xz}$  (blue solid curves) as defined in Ref. [55] multiplied by the cross sections for the reactions (a)  $K^- + p \rightarrow K^+ + \Xi^-$  and (b)  $K^- + p \rightarrow K^0 + \Xi^0$ . The numbers in the upper right corners represent the total energy of the system  $W$  in units of GeV.

only two other non-vanishing target-recoil asymmetries are related by  $K_{zz} = K_{xx}$  and  $K_{zx} = -K_{xz}$ .<sup>8</sup> We mention that  $\frac{d\sigma}{d\Omega}K_{xx}$  is proportional to the difference of the magnitude squared of the spin-non-flip and spin-flip matrix elements, while  $\frac{d\sigma}{d\Omega}K_{xz}$  is proportional to the real part of the product of the spin-non-flip matrix element with the complex conjugate of the spin-flip matrix element. Therefore, unlike the recoil asymmetry, these spin observables do not vanish even if the reaction amplitude is pure real or pure imaginary. This means that they are, like the cross section, much less sensitive to the complex nature of the phenomenological contact amplitude.

To gain some insight into the angular dependence exhibited by these target-recoil asymmetries in Fig. 10, we express them in terms of partial waves with  $L \leq 2$ , which gives

$$\begin{aligned} \frac{d\sigma}{d\Omega}K_{xx} &= |\alpha_{02}|^2 + \left[ |\alpha_1|^2 + 2 \operatorname{Re}(\alpha_{02}\tilde{\alpha}_2^*) \right] \cos^2 \theta \\ &+ |\tilde{\alpha}_2|^2 \cos^4 \theta - \left( |\beta_1|^2 + |\tilde{\beta}_2|^2 \cos^2 \theta \right) \sin^2 \theta \\ &+ 2 \operatorname{Re} \left[ \alpha_{02}\alpha_1^* + \alpha_1\tilde{\alpha}_2^* \cos^2 \theta \right. \\ &\quad \left. - \beta_1\tilde{\beta}_2^* \sin^2 \theta \right] \cos \theta, \end{aligned} \quad (16a)$$

$$\frac{d\sigma}{d\Omega}K_{xz} = 2 \operatorname{Re} \left[ \alpha_{02}\beta_1^* + \left( \alpha_1\tilde{\beta}_2^* + \tilde{\alpha}_2\beta_1^* \right) \cos^2 \theta \right]$$

$$+ \left( \alpha_{02}\tilde{\beta}_2^* + \alpha_1\beta_1^* \right) \cos \theta + \tilde{\alpha}_2\tilde{\beta}_2^* \cos^3 \theta \Big] \sin \theta. \quad (16b)$$

Note that the only difference between  $\frac{d\sigma}{d\Omega}K_{xx}$  given above and differential cross section given by Eq. (15) is the sign change of the terms involving  $\beta_L$ . These terms are, however, proportional to  $\sin^2 \theta$ . Therefore, this spin observable behaves like the differential cross section at very forward and backward angles, where  $\sin^2 \theta \ll 1$ . At  $\cos \theta = 0$ , the difference is due to the term of  $\pm|\beta_1|^2$ , which is a  $P$ -wave contribution in the spin-flip amplitude. Now, if we ignore the  $P$ -wave contribution — which is relatively very small in the neutral  $\Xi^0$  production over the nearly entire energy region considered as seen in Fig. 8(a) — it is immediate to see that Eq. (16a) involves only terms that are symmetric about  $\cos \theta = 0$ . We see in Fig. 10(b) that  $\frac{d\sigma}{d\Omega}K_{xx}$  exhibits roughly this symmetry.

For  $\frac{d\sigma}{d\Omega}K_{xz}$ , Eq. (16b) reveals a rather complicated angular dependence in general, and no particular feature is apparent in the results shown in Fig. 10, especially for the charged  $\Xi^-$  production process. Neglecting the  $P$ -wave contribution, Eq. (16b) reduces to  $\frac{d\sigma}{d\Omega}K_{xz} = \operatorname{Re} \left[ \left( \alpha_{02} + \tilde{\alpha}_2 \cos^2 \theta \right) \tilde{\beta}_2^* \right] \sin 2\theta$ , which is roughly the angular dependence exhibited in Fig. 10(b).

The present model predictions for the  $K^- + n \rightarrow K^0 + \Xi^-$  reaction are shown in Fig. 11. Here, the experimental data are extremely scarce, and they were not included in the present fitting procedure. Nevertheless, the current model is seen to predict those few data quite reasonably. Both the total and differential cross sections exhibit a very similar feature to those of the  $K^- + p \rightarrow K^+ + \Xi^-$  reaction with a noticeable small enhancement in the differential cross sections as seen in Fig. 11(b) for forward angles near  $\cos \theta = 0$  in  $K^- + n \rightarrow K^0 + \Xi^-$ . We see, however, some bigger differences in the individual amplitude

<sup>8</sup> Note that the symmetry of the reaction leads to  $K_{yy} = \pi_{\Xi}$  independent on the scattering angle  $\theta$  [54, 55]. Here,  $\pi_{\Xi}$  stands for the parity of the produced  $\Xi$  which is taken to be  $\pi_{\Xi} = +1$  for the ground state  $\Xi$ . Also,  $K_{xx} = K_{zz}|_{\cos \theta = \pm 1} = \pi_{\Xi}$ . The target asymmetry is identical to the recoil asymmetry in the present reaction. Therefore, we exhaust all the *independent* observables available in the reaction processes considered here.

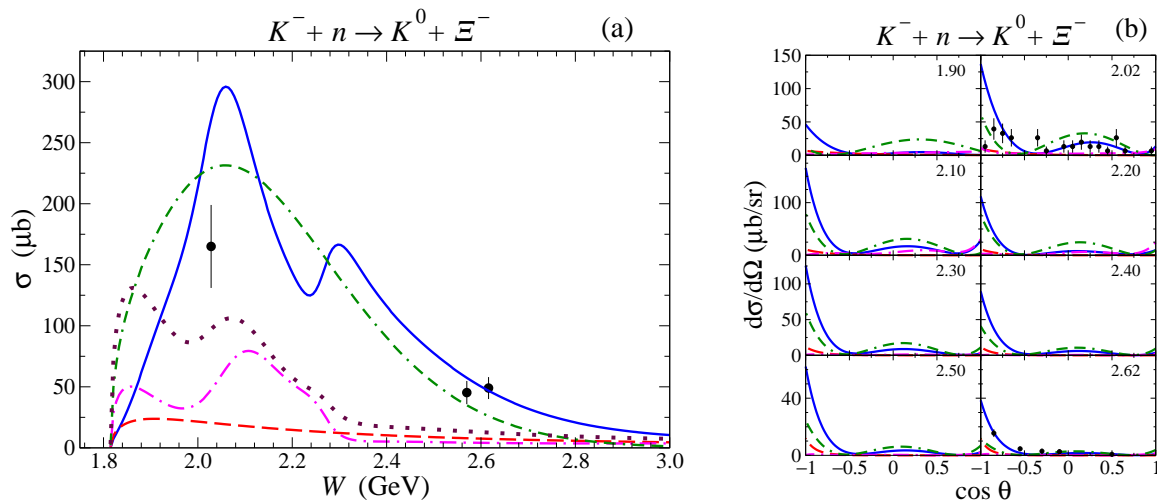


FIG. 11. (Color online) Same as Figs. 2(a) and 5 for the  $K^- + n \rightarrow K^0 + \Xi^-$  reaction. The experimental data are from Refs. [30, 38].

contributions, more clearly seen in the total cross sections that are given in Fig. 11(a). There, the  $\Sigma$  hyperon contribution is larger than the  $\Lambda$  contribution over the entire energy region up to  $W \sim 2.3$  GeV, in particular, at low energies near threshold. This is due to the absence of the strong destructive interference between the  $\Sigma(1385)$  and  $\Sigma(1192)$  (not shown), since the latter hyperon contribution is suppressed to a large extent compared to the case of  $K^- + p \rightarrow K^+ + \Xi^-$ . Moreover, there is a constructive interference with the  $\Lambda$  hyperon, which makes the sum of the hyperons contribution relatively large in the low energy region.

For completeness, we also show in Fig. 12 results for the  $K_L + p \rightarrow K^+ + \Xi^0$  reaction. Within the present model, the cross sections for this process simply differ by a factor of  $1/2$  from those shown in Fig. 11 for the  $K^- + n \rightarrow K^0 + \Xi^-$  reaction. We show the  $K_L$  results here because the creation of a high-intensity  $K_L$  beam currently being contemplated [71] may open up an entire new and exciting field of hyperon spectroscopy.

#### IV. CONCLUSION

In this work we have presented our analysis on the reaction of  $K^- + N \rightarrow K + \Xi$  within an effective Lagrangian approach that includes a phenomenological contact term to account for the final-state-interaction rescattering contribution of the reaction amplitude in the Bethe-Salpeter equation and for other possible (short-range) dynamics that are not explicitly taken into account in the model. By introducing this phenomenological contact term, we avoid the problems found in the usual implementations of tree-level effective Lagrangian approaches that need to phenomenologically suppress  $u$ -channel contributions dominating the high-energy behavior [50, 51]. In addition to the ground states  $\Lambda(1116)$  and  $\Sigma(1193)$ , the present

model also includes the  $\Lambda(1890)$ ,  $\Sigma(1385)$ ,  $\Sigma(2030)$ , and  $\Sigma(2250)$  resonance contributions.

The available total and differential cross sections, as well as the recoil asymmetry data, in both the  $K^- + p \rightarrow K^+ + \Xi^-$  and  $K^- + p \rightarrow K^0 + \Xi^0$  processes are well reproduced by the present model. We have found that the above-threshold resonances  $\Lambda(1890)$ ,  $\Sigma(2030)$ , and  $\Sigma(2250)$  are required to achieve a good fit quality for the data. Among them, the  $\Sigma(2030)$  resonance is the most critical one. This resonance affects not only the cross sections but also the recoil asymmetry. In addition, it also brings a model calculation of Ref. [24] into an agreement with the observed  $K^+\Xi^-$  invariant mass distribution in  $\Xi$  photoproduction [19]. The  $\Lambda(1890)$  is also required to improve the fit quality in the present model, especially in the energy dependence of the total cross sections of the charged  $\Xi^-$  production around  $W = 1.9$  GeV. The total cross section data in the charged  $\Xi^-$  production seems to indicate a bump structure at around  $W = 2.3$  GeV, which is accounted for by the  $\Sigma(2250)$  resonance with  $J^P = 5/2^-$  and a mass of 2265 MeV in the present model. More accurate data are required before a more definitive answer can be provided for the role of these two resonances. In this regard, the multi-strangeness hyperon production programs using an intense antikaon beam at J-PARC is of particular relevance in providing the much needed higher-precision data for the present reaction.

The present analysis also reveals a peculiar behavior of the total cross section data in the threshold-energy region of the  $K^+\Xi^-$  production channel, where the higher partial-waves ( $P$  and  $D$ ) dominate instead of the usual  $S$ -wave (cf. Fig. 7). If this behavior of the cross section data is corroborated in future experiments, it will cast serious doubts on the validity of model calculations that neglect higher partial-waves even for energies very close to threshold. This peculiar low-energy behavior of the total cross section in  $K^-$ -induced reaction seems to be

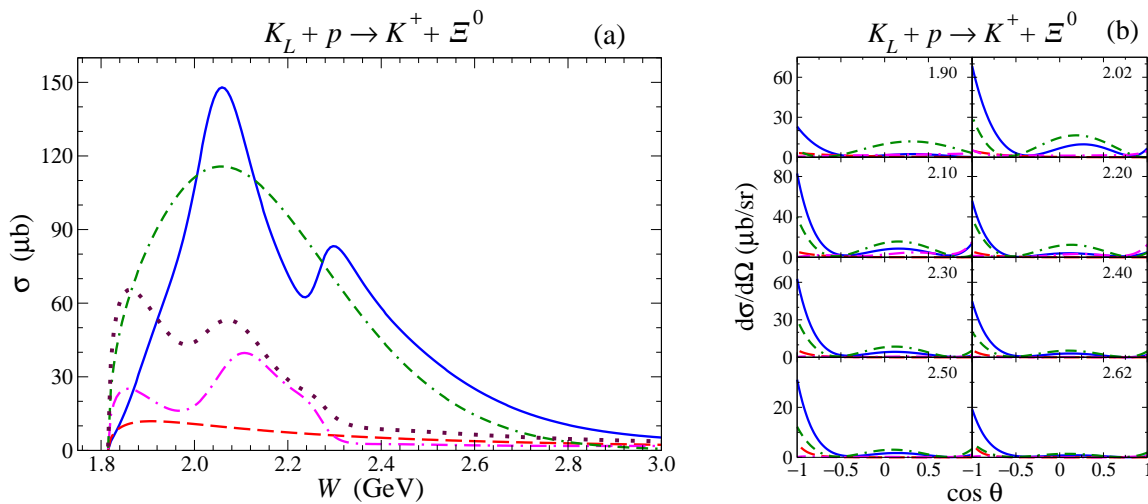


FIG. 12. (Color online) Same as Figs. 2(a) and 5 for the  $K_L + p \rightarrow K^+ + \Xi^0$  reaction.

present also in the  $\pi N$  and  $\eta N$  production channels, in addition to the  $K\Xi$  channel [53].

Apart from the recoil asymmetry, we have also predicted the target-recoil asymmetries for which there are currently no experimental data. In contrast to the recoil polarization — which are small — these observables are quite sizable and may help impose more stringent constraints on the model parameters. In principle, one requires the four independent observables calculated here to completely determine the reaction amplitude [55]. Of course, measurements of the spin observables, in particular, are challenging experimentally by any standard, but one may exploit the self-analyzing nature of the produced hyperon to help extract these observables [55, 72]. For the target-recoil asymmetry measurements, one requires a polarized target in addition to spin measurements of the produced  $\Xi$ . Polarized targets available at some of the world's major laboratories combined with the availability of intense beams make measuring these spin observables no longer out of reach. In fact, various single- and double-polarization observables in photoproduction reactions are currently being measured at major facilities such as JLab, ELSA, and MAMI, aiming at so-called complete experiment sets in order to model-independently determine the photoproduction amplitudes.

While it may perhaps not be entirely clear which role any particular resonance plays for the  $K^- + N \rightarrow K + \Xi$  reaction, the present and other calculations based on effective Lagrangians [50, 51], and also the unitarized chiral perturbation approach [52], seem to agree that some  $S = -1$  hyperon resonances seem to be required to reproduce the existing data. To pin down the role of a particular resonance among them requires more precise and complete data, in addition to more complete theoretical models. In any case, the present reaction is very well suited for studying  $S = -1$  hyperon resonances.

Finally, the present work is our first step toward building a more complete reaction theory to help analyze the

data and extract the properties of  $\Xi$  resonances in future experimental efforts in  $\Xi$  baryon spectroscopy. This is a complementary work to that of a model-independent analysis performed recently by the same authors [55] and will also help in analyzing the data to understand the production mechanisms of  $\Xi$  baryons.

## ACKNOWLEDGMENTS

We are grateful to D. A. Sharov for providing us with the digitized version of the data used in the present work. This work was partially supported by the National Research Foundation of Korea funded by the Korean Government (Grant No. NRF-2011-220-C00011). The work of Y.O. was also supported in part by the Ministry of Science, ICT, and Future Planning (MSIP) and the National Research Foundation of Korea under Grant No. NRF-2013K1A3A7A06056592 (Center for Korean J-PARC Users). The work of K.N. was also supported in part by the FFE-COSY Grant No. 41788390.

## Appendix

In this Appendix, we give the effective Lagrangians and phenomenological dressed baryon propagators from which the  $s$ - and  $u$ -channel amplitudes,  $M_s$  and  $M_u$  discussed in Sec. II, are constructed. We follow Refs. [23, 24, 73–75] and consider not only the spin-1/2 ground state  $\Lambda$  and  $\Sigma$  but also their respective excited states with spin up to 7/2. In the following we use the notations for the iso-doublet fields

$$\begin{aligned}
 N &= \begin{pmatrix} p \\ n \end{pmatrix}, & \Xi &= \begin{pmatrix} \Xi^0 \\ -\Xi^- \end{pmatrix}, \\
 K &= \begin{pmatrix} K^+ \\ K^0 \end{pmatrix}, & K_c &= \begin{pmatrix} \bar{K}^0 \\ -K^- \end{pmatrix},
 \end{aligned} \tag{A.1}$$

and for the iso-triplet fields

$$\Sigma = \begin{pmatrix} \Sigma^+ \\ \Sigma^0 \\ \Sigma^- \end{pmatrix}. \quad (\text{A.2})$$

We also introduce the auxiliary operators in Dirac space

$$D_{B'BM}^{1/2(\pm)} \equiv -\Gamma^{(\pm)} \left( \pm i\lambda + \frac{1-\lambda}{m_{B'} \pm m_B} \not{\partial} \right), \quad (\text{A.3a})$$

$$D_\nu^{3/2(\pm)} \equiv \Gamma^{(\mp)} \partial_\nu, \quad (\text{A.3b})$$

$$D_{\mu\nu}^{5/2(\pm)} \equiv -i\Gamma^{(\pm)} \partial_\mu \partial_\nu, \quad (\text{A.3c})$$

$$D_{\mu\nu\rho}^{7/2(\pm)} \equiv -\Gamma^{(\mp)} \partial_\mu \partial_\nu \partial_\rho, \quad (\text{A.3d})$$

where  $\Gamma^{(+)} \equiv \gamma_5$  and  $\Gamma^{(-)} \equiv 1$ . Here,  $m_B$  stands for the mass of the baryon  $B$ . The parameter  $\lambda$  has been introduced to interpolate between the pseudovector ( $\lambda = 0$ ) and the pseudoscalar ( $\lambda = 1$ ) couplings. Note that in the above equation the order of the subscript indices in  $D_{B'BM}^{1/2(\pm)}$  is important, i.e.,  $D_{B'BM}^{1/2(\pm)} \neq D_{BB'M}^{1/2(\pm)}$ .

The effective Lagrangians for spin-1/2 hyperons  $\Lambda$  and  $\Sigma$  (or their resonances) are, then, given by

$$\mathcal{L}_{\Lambda NK}^{1/2(\pm)} = g_{\Lambda NK} \bar{\Lambda} \left( D_{\Lambda NK}^{1/2(\pm)} \bar{K} \right) N + \text{H.c.}, \quad (\text{A.4a})$$

$$\mathcal{L}_{\Sigma NK}^{1/2(\pm)} = g_{\Sigma NK} \bar{\Sigma} \cdot \left( D_{\Sigma NK}^{1/2(\pm)} \bar{K} \right) \tau N + \text{H.c.}, \quad (\text{A.4b})$$

$$\mathcal{L}_{\Xi \Lambda K_c}^{1/2(\pm)} = g_{\Xi \Lambda K_c} \bar{\Xi} \left( D_{\Xi \Lambda K_c}^{1/2(\pm)} K_c \right) \Lambda + \text{H.c.}, \quad (\text{A.4c})$$

$$\mathcal{L}_{\Xi \Sigma K_c}^{1/2(\pm)} = g_{\Xi \Sigma K_c} \bar{\Xi} \tau \left( D_{\Xi \Sigma K_c}^{1/2(\pm)} K_c \right) \cdot \Sigma + \text{H.c.}, \quad (\text{A.4d})$$

where the superscripts  $\pm$  refer to the positive (+) and negative (−) relative parity of the baryons. Flavor SU(3) symmetry relates the coupling constants among the members of the octet  $J^P = 1/2^+$  ground state baryons and  $J^P = 0^-$  pseudoscalar mesons and we have

$$g_{\Lambda NK} = -g_8 \frac{1+2\alpha}{\sqrt{3}}, \quad (\text{A.5a})$$

$$g_{\Sigma NK} = g_8(1-2\alpha), \quad (\text{A.5b})$$

$$g_{\Xi \Lambda K_c} = -g_8 \frac{1-4\alpha}{\sqrt{3}}, \quad (\text{A.5c})$$

$$g_{\Xi \Sigma K_c} = -g_8, \quad (\text{A.5d})$$

where the empirical values are  $g_8 = g_{NN\pi} = 13.26$  and  $\alpha = 0.365$ , where  $\alpha$  is the  $F/D$  mixing parameter defined as  $\alpha = F/(D+F)$ .

For spin-3/2 hyperons, we have

$$\mathcal{L}_{\Lambda NK}^{3/2(\pm)} = \frac{g_{\Lambda NK}}{m_K} \bar{\Lambda}^\nu \left( D_\nu^{3/2(\pm)} \bar{K} \right) N + \text{H.c.}, \quad (\text{A.6a})$$

$$\mathcal{L}_{\Sigma NK}^{3/2(\pm)} = \frac{g_{\Sigma NK}}{m_K} \bar{\Sigma}^\nu \cdot \left( D_\nu^{3/2(\pm)} \bar{K} \right) \tau N + \text{H.c.}, \quad (\text{A.6b})$$

$$\mathcal{L}_{\Xi \Lambda K_c}^{3/2(\pm)} = \frac{g_{\Xi \Lambda K_c}}{m_K} \bar{\Xi} \left( D_\nu^{3/2(\pm)} K_c \right) \Lambda^\nu + \text{H.c.}, \quad (\text{A.6c})$$

$$\mathcal{L}_{\Xi \Sigma K_c}^{3/2(\pm)} = \frac{g_{\Xi \Sigma K_c}}{m_K} \bar{\Xi} \tau \left( D_\nu^{3/2(\pm)} K_c \right) \cdot \Sigma^\nu + \text{H.c.}, \quad (\text{A.6d})$$

where  $m_K$  denotes the kaon mass. For spin-5/2 hyperons [24, 76],

$$\mathcal{L}_{\Lambda NK}^{5/2(\pm)} = \frac{g_{\Lambda NK}}{m_K^2} \bar{\Lambda}^{\mu\nu} \left( D_{\mu\nu}^{5/2(\pm)} \bar{K} \right) N + \text{H.c.}, \quad (\text{A.7a})$$

$$\mathcal{L}_{\Sigma NK}^{5/2(\pm)} = \frac{g_{\Sigma NK}}{m_K^2} \bar{\Sigma}^{\mu\nu} \cdot \left( D_{\mu\nu}^{5/2(\pm)} \bar{K} \right) \tau N + \text{H.c.}, \quad (\text{A.7b})$$

$$\mathcal{L}_{\Xi \Lambda K_c}^{5/2(\pm)} = \frac{g_{\Xi \Lambda K_c}}{m_K^2} \bar{\Xi} \left( D_{\mu\nu}^{5/2(\pm)} K_c \right) \Lambda^{\mu\nu} + \text{H.c.}, \quad (\text{A.7c})$$

$$\mathcal{L}_{\Xi \Sigma K_c}^{5/2(\pm)} = \frac{g_{\Xi \Sigma K_c}}{m_K^2} \bar{\Xi} \tau \left( D_{\mu\nu}^{5/2(\pm)} K_c \right) \cdot \Sigma^{\mu\nu} + \text{H.c.}. \quad (\text{A.7d})$$

And, for spin-7/2 hyperons, we have [24, 76]

$$\mathcal{L}_{\Lambda NK}^{7/2(\pm)} = \frac{g_{\Lambda NK}}{m_K^3} \bar{\Lambda}^{\mu\nu\rho} \left( D_{\mu\nu\rho}^{7/2(\pm)} \bar{K} \right) N + \text{H.c.}, \quad (\text{A.8a})$$

$$\mathcal{L}_{\Sigma NK}^{7/2(\pm)} = \frac{g_{\Sigma NK}}{m_K^3} \bar{\Sigma}^{\mu\nu\rho} \cdot \left( D_{\mu\nu\rho}^{7/2(\pm)} \bar{K} \right) \tau N + \text{H.c.}, \quad (\text{A.8b})$$

$$\mathcal{L}_{\Xi \Lambda K_c}^{7/2(\pm)} = \frac{g_{\Xi \Lambda K_c}}{m_K^3} \bar{\Xi} \left( D_{\mu\nu\rho}^{7/2(\pm)} K_c \right) \Lambda^{\mu\nu\rho} + \text{H.c.}, \quad (\text{A.8c})$$

$$\mathcal{L}_{\Xi \Sigma K_c}^{7/2(\pm)} = \frac{g_{\Xi \Sigma K_c}}{m_K^3} \bar{\Xi} \tau \left( D_{\mu\nu\rho}^{7/2(\pm)} K_c \right) \cdot \Sigma^{\mu\nu\rho} + \text{H.c.}. \quad (\text{A.8d})$$

The coupling constants in the above Lagrangians corresponding to  $\Lambda$  and  $\Sigma$  resonances are free parameters adjusted to reproduce the existing data. For those resonances considered in the present work, they are given in Table III.

In the present work, all the meson-baryon-baryon vertices are obtained from the above Lagrangian. In addition, each vertex is multiplied by an off-shell form factor given by

$$f(p_r^2, m_r, \Lambda_r) = \left( \frac{n\Lambda_r^4}{n\Lambda_r^4 + (p_r^2 - m_r^2)^2} \right)^n, \quad (\text{A.9})$$

where  $p_r^2$  and  $m_r$  are the square of the 4-momentum and mass of the exchanged hyperon, respectively. The cutoff parameter  $\Lambda_r$  is chosen to have a common value  $\Lambda_r \equiv \Lambda = 900$  MeV for all the  $MBr$  vertices in order to keep the number of free parameters to a minimum. Also, we choose  $n = 1$ .

For the propagators of the dressed hyperons, we could in principle adopt the forms used in our previous work [24, 73–75]. However, in view of the limited amount of currently available data for the present reaction and the rather poor quality of these data, here we adopt the simpler forms as given in the following. For a spin-1/2 baryon propagator, we use

$$S_r^{1/2}(p_r) = \frac{1}{\not{p}_r - m_r + i\frac{\Gamma_r}{2}}, \quad (\text{A.10})$$

where  $\Gamma_r$  is the baryon width assumed to be constant, independent of energy. For a stable (ground state) baryon,  $\Gamma_r \rightarrow \epsilon$  with  $\epsilon$  being positive infinitesimal.



For spin-3/2, the dressed propagator reads in a schematic matrix notation

$$S_r^{3/2}(p_r) = \frac{1}{\not{p}_r - m_r + i\frac{\Gamma_r}{2}} \Delta, \quad (\text{A.11})$$

where  $\Delta$  is the Rarita-Schwinger tensor with elements

$$\Delta^{\mu\nu} = -g^{\mu\nu} + \frac{1}{3}\gamma^\mu\gamma^\nu + \frac{2p^\mu p^\nu}{3m_r^2} + \frac{\gamma^\mu p^\nu - p^\mu \gamma^\nu}{3m_r}. \quad (\text{A.12})$$

Similarly, the propagator for a spin-5/2 resonance is given by

$$S_r^{5/2}(p_r) = \frac{1}{\not{p}_r - m_r + i\frac{\Gamma_r}{2}} \Delta, \quad (\text{A.13})$$

where the elements of  $\Delta$  are [76]

$$\begin{aligned} \Delta_{\alpha_1\alpha_2}^{\beta_1\beta_2} &= \frac{1}{2} \left( \bar{g}_{\alpha_1}^{\beta_1} \bar{g}_{\alpha_2}^{\beta_2} + \bar{g}_{\alpha_1}^{\beta_2} \bar{g}_{\alpha_2}^{\beta_1} \right) - \frac{1}{5} \bar{g}_{\alpha_1\alpha_2} \bar{g}^{\beta_1\beta_2} \\ &\quad - \frac{1}{10} \left( \bar{\gamma}_{\alpha_1} \bar{\gamma}^{\beta_1} \bar{g}_{\alpha_2}^{\beta_2} + \bar{\gamma}_{\alpha_1} \bar{\gamma}^{\beta_2} \bar{g}_{\alpha_2}^{\beta_1} + \bar{\gamma}_{\alpha_2} \bar{\gamma}^{\beta_1} \bar{g}_{\alpha_1}^{\beta_2} \right. \\ &\quad \left. + \bar{\gamma}_{\alpha_2} \bar{\gamma}^{\beta_2} \bar{g}_{\alpha_1}^{\beta_1} \right), \end{aligned} \quad (\text{A.14})$$

with

$$\bar{g}^{\mu\nu} \equiv g^{\mu\nu} - \frac{p^\mu p^\nu}{m_r^2}, \quad \bar{\gamma}^\mu \equiv \gamma^\mu - \frac{p^\mu \not{p}}{m_r^2}. \quad (\text{A.15})$$

The propagator for a spin-7/2 resonance is given by

$$S_r^{7/2}(p_r) = \frac{1}{\not{p}_r - m_r + i\frac{\Gamma_r}{2}} \Delta, \quad (\text{A.16})$$

where the elements of  $\Delta$  are [76]

$$\begin{aligned} \Delta_{\alpha_1\alpha_2\alpha_3}^{\beta_1\beta_2\beta_3} &= \frac{1}{36} \sum_{P(\alpha), P(\beta)} \left( \bar{g}_{\alpha_1}^{\beta_1} \bar{g}_{\alpha_2}^{\beta_2} \bar{g}_{\alpha_3}^{\beta_3} - \frac{3}{7} \bar{g}_{\alpha_1}^{\beta_1} \bar{g}_{\alpha_2\alpha_3}^{\beta_2\beta_3} \bar{g}^{\beta_1\beta_3} \right. \\ &\quad \left. - \frac{3}{7} \bar{\gamma}_{\alpha_1} \bar{\gamma}^{\beta_1} \bar{g}_{\alpha_2}^{\beta_2} \bar{g}_{\alpha_3}^{\beta_3} + \frac{3}{35} \bar{\gamma}_{\alpha_1} \bar{\gamma}^{\beta_1} \bar{g}_{\alpha_2\alpha_3}^{\beta_2\beta_3} \right), \end{aligned}$$

- 
- [1] R. G. Edwards, N. Mathur, D. G. Richards, and S. J. Wallace (Hadron Spectrum Collaboration), Flavor structure of the excited baryon spectra from lattice QCD, *Phys. Rev. D* **87**, 054506 (2013).  
[2] G. P. Engel, C. B. Lang, D. Mohler, and A. Schäfer [BGR (Bern-Graz-Regensburg) Collaboration], QCD with two light dynamical chirally improved quarks: Baryons, *Phys. Rev. D* **87**, 074504 (2013).  
[3] D. J. Wilson, I. C. Cloet, L. Chang, and C. D. Roberts, Nucleon and Roper electromagnetic elastic and transition form factors, *Phys. Rev. C* **85**, 025205 (2012).  
[4] S. Capstick and W. Roberts, Quark models of baryon masses and decays, *Prog. Part. Nucl. Phys.* **45**, S241 (2000).

(A.17)

and the summation runs over all possible permutations of  $\{\alpha_1, \alpha_2, \alpha_3\}$  and of  $\{\beta_1, \beta_2, \beta_3\}$ .

To avoid an ambiguity in the relative phase between  $M_s + M_u$  and  $M_c$  in Eq. (11), we provide here the explicit expressions for the amplitudes  $M_s$  and  $M_u$  for the  $\Lambda(1116)$  exchange in the  $K^-(q) + N(p) \rightarrow K^+(q') + \Xi^-(p')$  reaction, i.e.,

$$M_s^\Lambda = \bar{u}_\Xi(\mathbf{p}') \Gamma_{\Xi^- K^+ \Lambda}^s(q') S_\Lambda^{1/2}(p_s) \Gamma_{\Lambda K^- N}^s(q) u_N(\mathbf{p}), \quad (\text{A.18a})$$

$$M_u^\Lambda = \bar{u}_\Xi(\mathbf{p}') \Gamma_{\Xi^- K^- \Lambda}^u(q) S_\Lambda^{1/2}(p_u) \Gamma_{\Lambda K^+ N}^u(q') u_N(\mathbf{p}), \quad (\text{A.18b})$$

where the nucleon index  $N$  stands for the proton and  $\Lambda$  stands for  $\Lambda(1116)$ ; the baryon Dirac spinors are normalized covariantly,  $\bar{u}_B u_B = 1$ , the intermediate four-momenta are  $p_s = p + q$  and  $p_u = p - q'$ , and the vertices are given as

$$\Gamma_{\Lambda K^- N}^s(q) = g_{\Lambda N K} \gamma^5 \left( \lambda - \frac{1 - \lambda}{m_\Lambda + m_N} \not{q} \right) f_s, \quad (\text{A.19a})$$

$$\Gamma_{\Xi K^+ \Lambda}^s(q') = g_{\Xi \Lambda K} \gamma^5 \left( \lambda + \frac{1 - \lambda}{m_\Xi + m_\Lambda} \not{q}' \right) f_s, \quad (\text{A.19b})$$

$$\Gamma_{\Lambda K^+ N}^u(q') = g_{\Lambda N K} \gamma^5 \left( \lambda + \frac{1 - \lambda}{m_\Lambda + m_N} \not{q}' \right) f_u, \quad (\text{A.19c})$$

$$\Gamma_{\Xi K^- \Lambda}^u(q) = g_{\Xi \Lambda K} \gamma^5 \left( \lambda - \frac{1 - \lambda}{m_\Xi + m_\Lambda} \not{q} \right) f_u, \quad (\text{A.19d})$$

where  $\lambda$  describes the linear interpolation between pseudoscalar ( $\lambda = 1$ ) and pseudovector ( $\lambda = 0$ ) couplings; the off-shell form factors are given by [see Eq. (A.9)]

$$f_s = f(p_s^2, m_\Lambda, \Lambda_\Lambda), \quad (\text{A.20a})$$

$$f_u = f(p_u^2, m_\Lambda, \Lambda_\Lambda), \quad (\text{A.20b})$$

and the values of  $g_{\Lambda N K}$ ,  $g_{\Xi \Lambda K}$ , and  $\lambda$  are found in Table III.

- [5] M. Ronniger and B. C. Metsch, Effects of a spin-flavour dependent interaction on the baryon mass spectrum, *Eur. Phys. J. A* **47**, 162 (2011).  
[6] Y. Oh,  $\Xi$  and  $\Omega$  baryons in the Skyrme model, *Phys. Rev. D* **75**, 074002 (2007).  
[7] E. Oset and A. Ramos, Dynamically generated resonances from the vector octet-baryon octet interaction, *Eur. Phys. J. A* **44**, 445 (2010).  
[8] M. Mai, P. C. Bruns, and U.-G. Meissner, Pion photoproduction off the proton in a gauge-invariant chiral unitary framework, *Phys. Rev. D* **86**, 094033 (2012).  
[9] R. Arndt, W. Briscoe, I. Strakovsky, and R. Workman, Partial-wave analysis and baryon spectroscopy, *Eur. Phys. J. A* **35**, 311 (2008).

- [10] A. V. Anisovich, R. Beck, E. Klempt, V. A. Nikonov, A. V. Sarantsev, and U. Thoma, Properties of baryon resonances from a multichannel partial wave analysis, *Eur. Phys. J. A* **48**, 15 (2012).
- [11] G. Y. Chen, S. S. Kamalov, S. N. Yang, D. Drechsel, and L. Tiator, Nucleon resonances in  $\pi N$  scattering up to energies  $\sqrt{s} \leq 2.0$  GeV, *Phys. Rev. C* **76**, 035206 (2007).
- [12] L. Tiator, S. S. Kamalov, S. Ceci, G. Y. Chen, D. Drechsel, A. Svarc, and S. N. Yang, Singularity structure of the  $\pi N$  scattering amplitude in a meson-exchange model up to energies  $W \leq 2.0$  GeV, *Phys. Rev. C* **82**, 055203 (2010).
- [13] V. Shklyar, H. Lenske, and U. Mosel,  $\eta$ -meson production in the resonance energy region, *Phys. Rev. C* **87**, 015201 (2013).
- [14] A. Matsuyama, T. Sato, and T.-S. H. Lee, Dynamical coupled-channel model of meson production reactions in the nucleon resonance region, *Phys. Rep.* **439**, 193 (2007).
- [15] H. Kamano, S. X. Nakamura, T.-S. H. Lee, and T. Sato, Extraction of  $P_{11}$  resonances from  $\pi N$  data, *Phys. Rev. C* **81**, 065207 (2010).
- [16] D. Rönchen, M. Döring, F. Huang, H. Haberzettl, J. Haidenbauer, C. Hanhart, S. Krewald, U. G. Meißner, and K. Nakayama, Coupled-channel dynamics in the reactions  $\pi N \rightarrow \pi N$ ,  $\eta N$ ,  $K\Lambda$ ,  $K\Sigma$ , *Eur. Phys. J. A* **49**, 44 (2013).
- [17] K. A. Olive *et al.* (Particle Data Group), Review of particle physics, *Chin. Phys. C* **38**, 090001 (2014).
- [18] E. Klempt and J.-M. Richard, Baryon spectroscopy, *Rev. Mod. Phys.* **82**, 1095 (2010).
- [19] L. Guo *et al.* (CLAS Collaboration), Cascade production in the reactions  $\gamma p \rightarrow K^+ K^+(X)$  and  $\gamma p \rightarrow K^+ K^+ \pi^-(X)$ , *Phys. Rev. C* **76**, 025208 (2007).
- [20] V. Flaminio, W. G. Moorhead, D. R. O. Morrison, and N. Rivoire (High-Energy Reactions Analysis Group), Compilation of cross-sections. II.  $K^+$  and  $K^-$  induced reactions, 1983, CERN Report No. CERN-HERA-83-02.
- [21] H.-Y. Ryu, A. Hosaka, H. Haberzettl, H.-C. Kim, K. Nakayama, and Y. Oh, Hadronic description for Omega baryon photoproduction, *PoS Hadron2013*, 140 (2013), [arXiv:1401.3804].
- [22] A. Afanasev *et al.* (The Very Strange Collaboration), Photoproduction of the very strangest baryons on a proton target in CLAS12, 2012, JLab. Report No. JLAB-PR-12-008.
- [23] K. Nakayama, Y. Oh, and H. Haberzettl, Photoproduction of  $\Xi$  off nucleons, *Phys. Rev. C* **74**, 035205 (2006).
- [24] J. K. S. Man, Y. Oh, and K. Nakayama, Role of high-spin hyperon resonances in the reaction of  $\gamma p \rightarrow K^+ K^+ \Xi^-$ , *Phys. Rev. C* **83**, 055201 (2011).
- [25] J. K. Ahn, Production of  $\Xi^*$  resonances in the  $K^- p$  interaction at J-PARC, *J. Korean Phys. Soc.* **49**, 2276 (2006).
- [26] H. Takahashi,  $S = -3$  physics at J-PARC, *Nucl. Phys. A* **914**, 553 (2013).
- [27] W. Erni *et al.* (The PANDA Collaboration), Physics performance report for PANDA: Strong interaction studies with antiprotons, arXiv:0903.3905.
- [28] G. M. Pjerrou, D. J. Prowse, P. Schlein, W. E. Slater, D. H. Stork, and H. K. Ticho, Resonance in the  $(\Xi\pi)$  System at 1.53 GeV, *Phys. Rev. Lett.* **9**, 114 (1962).
- [29] D. D. Carmony, G. M. Pjerrou, P. E. Schlein, W. E. Slater, D. H. Stork, and H. K. Ticho, Properties of  $\Xi$  hyperons, *Phys. Rev. Lett.* **12**, 482 (1964).
- [30] J. P. Berge, P. Eberhard, J. R. Hubbard, D. W. Merrill, J. Button-Shafer, F. T. Solmitz, and M. L. Stevenson, Some properties of  $\Xi^-$  and  $\Xi^0$  hyperons produced in  $K^- p$  interactions between 1.05 and 1.7 BeV/c, *Phys. Rev.* **147**, 945 (1966).
- [31] M. Haque *et al.* [Birmingham-Glasgow-London(I.C.)-Oxford-Rutherford Collaboration], Reactions  $K^- p \rightarrow$  Hyperon + Meson at 3.5 GeV/c, *Phys. Rev.* **152**, 1148 (1966).
- [32] G. W. London, R. R. Rau, N. P. Samios, S. S. Yamamoto, M. Goldberg, S. Lichtman, M. Prime, and J. Leitner,  $K^- p$  interaction at 2.24 BeV/c, *Phys. Rev.* **143**, 1034 (1966).
- [33] T. G. Trippe and P. E. Schlein, Partial-wave analysis of  $K^- p \rightarrow \Xi^- K^+$  at 2 GeV/c, *Phys. Rev.* **158**, 1334 (1967).
- [34] W. P. Trower, J. R. Ficenece, R. I. Hulsizer, J. Lathrop, J. N. Snyder, and W. P. Swanson, Some two-body final states of  $K^- p$  interactions at 1.33 GeV/c, *Phys. Rev.* **170**, 1207 (1968).
- [35] D. W. Merrill and J. Button-Shafer, Properties of the  $\Xi^-$  and the  $\Xi(1817)$  from  $K^- p$  Interactions above 1.7 BeV/c, *Phys. Rev.* **167**, 1202 (1968).
- [36] G. Burgun *et al.*, Resonance formation in the reactions  $K^- p \rightarrow K^+ \Xi^-$  and  $K^- p \rightarrow K^0 \Xi^0$  in the mass region from 1915 to 2168 MeV, *Nucl. Phys. B* **8**, 447 (1968).
- [37] P. M. Dauber, J. P. Berge, J. R. Hubbard, D. W. Merrill, and R. A. Muller, Production and decay of cascade hyperons, *Phys. Rev.* **179**, 1262 (1969).
- [38] J. C. Scheuer *et al.* (S.A.B.R.E. Collaboration), Experimental study of two-body and quasi-two-body reactions in  $K^- n$  interactions at 3 GeV/c, *Nucl. Phys. B* **33**, 61 (1971).
- [39] A. de Bellefon *et al.*, Channel cross-sections of  $K^- p$  reactions from 1.26 to 1.84 GeV/c, *Nuovo Cim. A* **7**, 567 (1972).
- [40] J. R. Carlson, H. F. Davis, D. E. Jauch, N. D. Sossong, and R. Ellsworth, Measurement of neutral cascade production from, *Phys. Rev. D* **7**, 2533 (1973).
- [41] R. Rader *et al.*, The reaction  $K^- p \rightarrow \Lambda \eta$  from 0.80 to 1.84 GeV/c, *Nuovo Cim. A* **16**, 178 (1973).
- [42] J. Griselin *et al.*,  $K^- p$  cross sections between 1.1 and 1.4 GeV/c, *Nucl. Phys. B* **93**, 189 (1975).
- [43] E. Briefel *et al.*, Search for  $\Xi^*$  production in  $K^- p$  reactions at 2.87 GeV/c, *Phys. Rev. D* **16**, 2706 (1977).
- [44] O. Dumbrajs, R. Koch, H. Pilkuhn, G. C. Oades, H. Behrens, J. J. de Swart, and P. Kroll, Compilation of coupling constants and low-energy parameters: 1982-edition, *Nucl. Phys. B* **216**, 277 (1983).
- [45] M. E. Ebel and P. B. James, Peripheral model for  $\Xi^-$  associated productions, *Phys. Rev.* **153**, 1694 (1967).
- [46] P. B. James, Baryon exchange in  $\Xi$  production processes, *Phys. Rev.* **158**, 1617 (1967).
- [47] B. K. Agarwal, C. P. Singh, K. J. Narain, and A. B. Saxena,  $K^- p \rightarrow K^+ \Xi^-$  process in the two-meson-exchange peripheral model, *J. Phys. A*, **4**, L52 (1971).
- [48] K. L. Mir and J. K. Storrow, Hyperon-exchange reactions at high energies. III. Backward  $KN \rightarrow \Xi K$  scattering, *J. Phys. G* **8**, 465 (1982).
- [49] C. B. Dover and A. Gal,  $\Xi$  hypernuclei, *Ann. Phys. (N.Y.)* **146**, 309 (1983).
- [50] D. A. Sharov, V. L. Korotkikh, and D. E. Lansky, Phenomenological model for the  $\bar{K}N \rightarrow K\Xi$  reaction, *Eur.*

- Phys. J. A **47**, 109 (2011).
- [51] R. Shyam, O. Scholten, and A. W. Thomas, Production of a Cascade hyperon in the  $K^-$ -proton interaction, Phys. Rev. C **84**, 042201 (2011).
- [52] V. K. Magas, A. Feijoo, and A. Ramos, The  $K^-N \rightarrow K\Xi$  reaction in coupled channel chiral models up to next-to-leading order, AIP Conf. Proc. **1606**, 208 (2014).
- [53] H. Kamano, S. X. Nakamura, T.-S. H. Lee, and T. Sato, Dynamical coupled-channels model of  $K^-p$  reactions (I): Determination of partial-wave amplitudes, Phys. Rev. C **90**, 065204 (2014).
- [54] K. Nakayama, Y. Oh, and H. Haberzettl, Model-independent determination of the parity of  $\Xi$  hyperons, Phys. Rev. C **85**, 042201(R) (2012).
- [55] B. Jackson, Y. Oh, H. Haberzettl, and K. Nakayama, Model-independent aspects of the reaction  $\bar{K} + N \rightarrow K + \Xi$ , Phys. Rev. C **89**, 025206 (2014).
- [56] H. Zhang, J. Tulpan, M. Shrestha, and D. M. Manley, Partial-wave analysis of  $\bar{K}N$  scattering reactions, Phys. Rev. C **88**, 035204 (2013).
- [57] H. Zhang, J. Tulpan, M. Shrestha, and D. M. Manley, Multichannel parametrization of  $\bar{K}N$  scattering amplitudes and extraction of resonance parameters, Phys. Rev. C **88**, 035205 (2013).
- [58] Y. Yamamoto, T. Motoba, T. Fukuda, M. Takahashi, and K. Ikeda, Formation and transition of strangeness  $S = -2$  nuclear systems, Prog. Theor. Phys. Suppl. **117**, 281 (1994).
- [59] S. Tadokoro, H. Kobayashi, and Y. Akaishi,  $\Xi^-$ -hypernuclear states in heavy nuclei, Phys. Rev. C **51**, 2656 (1995).
- [60] M. Kohno and S. Hashimoto,  $\Xi$ -nucleus potential and ( $K^-$ ,  $K^+$ ) inclusive spectrum at  $\Xi^-$  production threshold region, Prog. Theor. Phys. **123**, 157 (2010).
- [61] K. Nakayama and W. G. Love, Spin structure of spin-1/2 baryon and spinless meson production amplitudes in photonic and hadronic reactions, Phys. Rev. C **72**, 034603 (2005).
- [62] M. Döring and K. Nakayama, On the cross section ratio  $\sigma_n/\sigma_p$  in  $\eta$  photoproduction, Phys. Lett. B **683**, 145 (2010).
- [63] A. Ramos and E. Oset, The role of vector-baryon channels and resonances in the  $\gamma p \rightarrow K^0\Sigma^+$  and  $\gamma n \rightarrow K^0\Sigma^0$  reactions near the  $K^*\Lambda$  threshold, Phys. Lett. B **727**, 287 (2013).
- [64] H.-Y. Ryu, A. I. Titov, A. Hosaka, and H.-C. Kim,  $\phi$  photoproduction with coupled-channel effects, Prog. Theor. Exp. Phys. **2014**, 023D03 (2014).
- [65] H. Ryu, A. Hosaka, H.-C. Kim, and A. I. Titov, Photoproduction of phi meson near the threshold, Int. J. Mod. Phys. Conf. Ser. **26**, 1460055 (2014).
- [66] R. Shyam and O. Scholten, Photoproduction of  $\eta$  mesons within a coupled-channels  $K$ -matrix approach, Phys. Rev. C **78**, 065201 (2008).
- [67] D. Plümpfer, J. Flender, and M. F. Gari, Nucleon-nucleon interaction from meson exchange and nucleonic structure, Phys. Rev. C **49**, 2370 (1994).
- [68] D. Drechsel, S. S. Kamalov, and L. Tiator, Unitary isobar model - MAID2007, Eur. Phys. J. A **34**, 69 (2007).
- [69] S. H. Razavi and K. Nakayama, Complex phase structure of the  $T$ -matrix amplitude and unitary and analytic isobar model, (in preparation).
- [70] L. Wolfenstein, Polarization of fast nucleons, Ann. Rev. Nucl. Sci. **6**, 43 (1956).
- [71] M. Amaryan, (private communication).
- [72] K. Moriya *et al.* (CLAS Collaboration), Spin and parity measurement of the  $\Lambda(1405)$  baryon, Phys. Rev. Lett. **112**, 082004 (2014).
- [73] K. Nakayama and H. Haberzettl, Consistent analysis of the reactions  $\gamma p \rightarrow p\eta'$  and  $pp \rightarrow pp\eta'$ , Phys. Rev. C **69**, 065212 (2004).
- [74] K. Nakayama and H. Haberzettl, Analyzing  $\eta'$  photoproduction data on the proton at energies of 1.5–2.3 GeV, Phys. Rev. C **73**, 045211 (2006).
- [75] K. Nakayama, Y. Oh, and H. Haberzettl, Combined analysis of  $\eta$  meson hadro- and photo-production off nucleons, J. Korean Phys. Soc. **59**, 224 (2011).
- [76] S.-J. Chang, Lagrange formulation for systems with higher spin, Phys. Rev. **161**, 1308 (1967).